

# Three Quantum-Geometric Contributions to Cubic Orbital Magnetization

Tohid Farajollahpour<sup>1,2,\*</sup>

<sup>1</sup>*Department of Physics, Norwegian University of Science and Technology (NTNU), NO-7491 Trondheim, Norway*

<sup>2</sup>*Department of Physics, Brock University, St. Catharines, Ontario L2S 3A1, Canada*

In noncentrosymmetric metals such as  $C_{3v}$  topological-insulator surfaces, moiré heterobilayers, and zincblende crystals, point-group symmetry can forbid the linear and quadratic electric-field-induced orbital magnetization, leaving the cubic response as the leading signal. Using a Ward-complete finite-momentum cubic Kubo kernel with an antisymmetric linear-in- $q$  projection, we show that the dc response separates into three quantum-geometric channels. These are a mixed electric-magnetic positional-shift quadrupole, a quantum-metric drift term, and an orbital-moment octupole. The three contributions share the same point-group symmetry but differ in their lifetime, frequency, and gate fingerprints. For a warped  $C_{3v}$  surface the metric channel obeys the cutoff-independent law  $\bar{\chi}_G \propto \mu^{-2}$ . We propose third-harmonic magneto-optical Kerr spectroscopy as an experimental route.

**Introduction.** Quantum geometry of Bloch states has become a unifying language for nonlinear responses in noncentrosymmetric crystals [1–4]. At second order, the Berry-curvature dipole produces the nonlinear Hall effect [5, 6], while the quantum metric gives a distinct intrinsic channel recently observed in topological anti-ferromagnets [7, 8]. At third order, quantum-geometric multipoles such as the quantum-metric quadrupole [9, 10], Berry-curvature quadrupole [11–14], and Berry-connection polarizability [15, 16] generate cubic Hall and longitudinal currents [17–22]. Much less is known for nonlinear orbital magnetization. Recently, Qiang *et al.* showed that a quadratic electric-field-induced orbital magnetization is governed by a quantum Christoffel symbol [23], and Qian *et al.* detected this response by second-harmonic magneto-optical Kerr spectroscopy in WTe<sub>2</sub> [24]. In several central noncentrosymmetric platforms, however, symmetry removes the quadratic magnetization channel. This occurs on  $C_{3v}$  topological-insulator surfaces such as Bi<sub>2</sub>Se<sub>3</sub> and Bi<sub>2</sub>Te<sub>3</sub> [25–29], in hexagonal moiré platforms with  $C_{3v}$  or  $D_3$  selection rules [30–35], and in zincblende-type tetrahedral ( $T_d$ ) crystals [36, 37]. In these cases the relevant axial representation first appears in the symmetric cubic product of the electric field [38–40], so the leading order of orbital-magnetization response is genuinely cubic.

In this Letter, we develop such a theory from a gauge-invariant finite-momentum cubic Kubo response. The antisymmetric linear-in- $q$  projection that isolates magnetization from transport currents yields three independent dc contributions, a mixed electric-magnetic positional-shift quadrupole  $\beta^{(H)}$ , a metric or Christoffel-drift term  $\beta^{(G)}$ , and an orbital-moment octupole transport term  $\beta^{(tr)}$ . The metric term is the cubic analogue of the quadratic quantum-Christoffel mechanism [23, 24], and the transport term extends the established semiclassical orbital-moment response. The genuinely new contribution is the mixed quadrupole, which has no quadratic counterpart because it draws on the second-order field-induced orbital moment built from simultaneous electric

and magnetic interband mixing. The Kubo construction identifies the mixed-quadrupole and metric contributions only after the Ward-complete finite- $q$  kernel and contact terms are combined. The three contributions transform identically under the point group but remain independent operators with distinct lifetime, frequency, and gate fingerprints, which provide the experimental handles for third-harmonic magneto-optical Kerr spectroscopy. In the continuum benchmark the mixed quadrupole still requires a microscopic magnetic-coupling prescription, so the metric term gives the cleanest closed prediction.

**Cubic-order magnetization and the multipole hierarchy.** This selection rule can be seen explicitly on the  $C_{3v}$  topological-insulator surface. The out-of-plane magnetization  $M_z$  transforms as the axial irrep  $A_2$ , whereas an in-plane electric field  $\mathbf{E} = E_0(\cos\phi, \sin\phi, 0)$  transforms as the two-dimensional irrep  $E$ . Since  $\text{Sym}^1(E) = E$  and  $\text{Sym}^2(E) = A_1 \oplus E$ , while  $\text{Sym}^3(E) = A_1 \oplus A_2 \oplus E$ , neither the linear nor the quadratic response can generate  $M_z$  and the leading allowed term is cubic. This gives the angular fingerprint  $M_z^{(3)} \propto E_0^3 \cos 3\phi$  or  $E_0^3 \sin 3\phi$ , depending on the choice of crystalline axes [Fig. 1(a)] [38–40]. Equivalently, the electric-field-induced orbital magnetization admits the nonlinear expansion  $M_a(\mathbf{E}) = \chi_{ab}^{(1)} E_b + \chi_{abc}^{(2)} E_b E_c + \chi_{abcd}^{(3)} E_b E_c E_d + \dots$ , where point-group symmetry selects which response tensors are nonzero [38–40]. These systems therefore realize a symmetry filter,  $\chi^{(1)} = \chi^{(2)} = 0$  but  $\chi^{(3)} \neq 0$ , for the relevant axial magnetization.

When  $\chi^{(2)}$  is symmetry allowed, as in orthorhombic  $T_d$ -phase WTe<sub>2</sub> and MoTe<sub>2</sub> with  $C_{2v}$  point symmetry [23, 24, 41, 42], the cubic signal coexists with the quadratic channel and must be isolated by its harmonic, lifetime, and frequency-mixing structure. In the symmetry-filtered  $C_{3v}$ ,  $D_3$ , and zincblende cases, by contrast, it is the leading magnetization response. The analogy with third-order transport multipoles [9–12, 15–22, 43, 44] raises the central question of whether orbital magnetization has its own multipole hierarchy and how the individual components can be separated experimen-

tally.

*Cubic Kubo kernel and  $q$ -linear projection.* We compute the cubic magnetization from the antisymmetric  $q$ -linear part of a finite-momentum current response [45–48], rather than from the strictly uniform  $\mathbf{q} = 0$  photocurrent tensor used in nonlinear optical response [49–52]. The starting point is the minimally coupled inverse Green function  $G^{-1}(K, A) = i\nu_n + \mu - h(\mathbf{k} - e\mathbf{A}/\hbar)$ , where  $K = (\mathbf{k}, i\nu_n)$  is the internal momentum-Matsubara label, with  $\mathbf{k}$  the crystal momentum and  $\nu_n$  a fermionic Matsubara frequency. Here  $\mu$  is the chemical potential,  $h(\mathbf{k})$  represents the Bloch Hamiltonian, and  $\mathbf{A}$  is the electromagnetic vector potential, with the Peierls substitution taken in its long-wavelength limit. The corresponding generating functional is

$$W[\mathbf{A}] = -T \text{Tr} \ln[-G^{-1}(A)], \quad (1)$$

with  $T$  the temperature and the trace running over  $K$  and the internal indices. The current density follows as  $j_a(Q) = -(1/V) \delta W / \delta A_a(-Q)$ , with  $V$  the system volume, and three further functional derivatives give the cubic current kernel

$$\begin{aligned} \tilde{K}_{a,jkl}^R(Q, Q_1, Q_2, Q_3) \\ = -\frac{1}{V} \frac{\delta^4 W}{\delta A_a(-Q) \delta A_j(Q_1) \delta A_k(Q_2) \delta A_l(Q_3)} \Big|_{A=0}, \quad (2) \end{aligned}$$

where  $Q_1, Q_2, Q_3$  are external four-momenta on the input legs,  $Q = Q_1 + Q_2 + Q_3$  enforces energy and momentum conservation, and the ordered retarded branch is obtained after the input ordering and paired frequency labels are fixed [48]. Minimal coupling generates, in addition to the paramagnetic vertex  $\Gamma_i^{(1)} = (e/\hbar)\partial_i h$ , the diamagnetic vertices  $\Gamma^{(2)}$ ,  $\Gamma^{(3)}$ , and  $\Gamma^{(4)}$ , involving the second through fourth derivatives of  $h$ . Keeping all box and contact terms gives a 26-term Ward-complete kernel. Omitting the contact terms, or differentiating only the propagator routing while dropping finite- $q$  Peierls vertex derivatives before the Ward-complete  $q \rightarrow 0$  limit, produces spurious longitudinal pieces and a gauge-dependent magnetization projection [48].

The orbital magnetization is obtained from the antisymmetric part of the current that is linear in the external wave vector  $\mathbf{q}$ . Using  $\mathbf{j}^{(M)} = \nabla \times \mathbf{M}$  together with the frequency-domain relation  $E_j(\omega_r) = i\omega_r A_j(\omega_r)$  on each input leg, with  $\omega_r$  the frequency on leg  $r$ , we define

$$\tilde{\beta}_{c,jkl}(\Omega, \omega_1, \omega_2, \omega_3) = \frac{\epsilon_{cab}}{4\omega_1\omega_2\omega_3} \left[ \frac{\partial \tilde{K}_{a,jkl}^R}{\partial q_b} - \frac{\partial \tilde{K}_{b,jkl}^R}{\partial q_a} \right]_{\mathbf{q}=0}, \quad (3)$$

so that  $M_c = \tilde{\beta}_{c,jkl} E_j E_k E_l$  identifies  $\tilde{\beta}_{c,jkl}$  as the ordered cubic magnetization kernel. Equation (3) is the step that separates a magnetization observable from the usual transport response evaluated at strictly  $\mathbf{q} = 0$ .

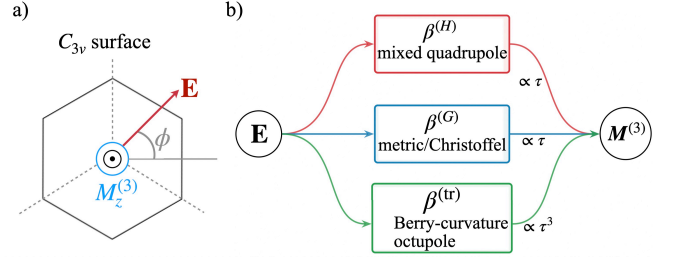


FIG. 1. Symmetry filter and three-channel decomposition of cubic orbital magnetization. (a) In the  $C_{3v}$  example, the lower-order axial response is forbidden and the leading signal is the threefold cubic harmonic  $\propto E_0^3 \cos 3\phi$ , with the phase fixed by the crystalline axes. (b) The dc tensor decomposes into three quantum-geometric channels.

The calculation is performed at finite external four-momenta, projected with Eq. (3), and then reduced to the low-frequency single-relaxation-time form. Within the clean noninteracting theory the Ward identities force  $\tilde{K}_{a,jkl}^R$  to carry an overall factor  $\omega_1\omega_2\omega_3$  that cancels the  $1/(\omega_1\omega_2\omega_3)$  in Eq. (3), leaving a finite dc limit for the electric-field tensor [48].

*Three quantum-geometric contributions.* For the non-magnetic time-reversal-symmetric case considered here, the dc, single-relaxation-time reduction of Eq. (3) gives a cubic magnetization tensor with three independent quantum-geometric contributions [Fig. 1(b)],

$$\tilde{\beta}_{ijkl}^{\text{dc}} = \beta_{ijkl}^{(H)} + \beta_{ijkl}^{(G)} + \beta_{ijkl}^{(\text{tr})}, \quad (4)$$

where

$$\beta_{ijkl}^{(H)} = \frac{e^3\tau}{\hbar} \sum_{\nu} \int_{\text{BZ}} \frac{d^d k}{(2\pi)^d} f_0(\varepsilon_{\nu}) \partial_l H_{ijk}^{\nu}, \quad (5a)$$

$$\beta_{ijkl}^{(G)} = \frac{e^3\tau}{2\hbar} \sum_{\nu} \int_{\text{BZ}} \frac{d^d k}{(2\pi)^d} (\partial_l m_i^{\nu}) \mathcal{G}_{jk}^{\nu} f_0'(\varepsilon_{\nu}), \quad (5b)$$

$$\beta_{ijkl}^{(\text{tr})} = \frac{e^3\tau^3}{\hbar^3} \sum_{\nu} \int_{\text{BZ}} \frac{d^d k}{(2\pi)^d} f_0(\varepsilon_{\nu}) \partial_j \partial_k \partial_l m_i^{\nu}. \quad (5c)$$

Here  $\tau$  is the relaxation time,  $\varepsilon_{\nu}$  is the band energy for the band  $\nu$  and  $f_0(\varepsilon_{\nu})$  is the equilibrium Fermi function with  $f_0' \equiv \partial_{\varepsilon} f_0$ . The intrinsic orbital magnetic moment  $m_i^{\nu}$  is

$$m_i^{\nu} = \frac{e}{2\hbar} \epsilon_{iab} \text{Im} \langle \partial_a u_{\nu} | (\varepsilon_{\nu} - h) | \partial_b u_{\nu} \rangle, \quad (6)$$

the gap-weighted quantum metric  $\mathcal{G}_{jk}^{\nu}$  is

$$\mathcal{G}_{jk}^{\nu} = 2 \sum_{\mu \neq \nu} \frac{\text{Re} A_{\nu\mu}^j A_{\mu\nu}^k}{\varepsilon_{\nu} - \varepsilon_{\mu}}, \quad (7)$$

and the symmetrized mixed electric-magnetic positional-shift contribution to the second-order field-induced orbital moment is

$$\delta m_{\nu,i}^{(2)} = e^2 H_{ijk}^{\nu} E_j E_k, \quad H_{ijk}^{\nu} = -\frac{1}{2} (\mathcal{Q}_{jki}^{\nu} + \mathcal{Q}_{kji}^{\nu}), \quad (8)$$

where  $A_{\nu\mu}^a = i\langle u_\nu | \partial_a u_\mu \rangle$  is the interband Berry connection and  $u_\nu$  the cell-periodic Bloch eigenstate. The explicit gauge-covariant construction of  $\mathcal{Q}_{\alpha\beta\gamma}^\nu$  from electric and magnetic interband mixing amplitudes is given in the Supplemental Material [48].

Equations (5) have a simple multipole interpretation. The  $\beta^{(H)}$  contribution is the occupied-state dipole of a mixed electric-magnetic quadrupolar correction to the local orbital moment. The  $\beta^{(G)}$  term is a Fermi-surface metric drift, or equivalently  $\beta_{ijkl}^{(G)} = -(e^3\tau/2\hbar) \sum_\nu \int_{\text{BZ}} m_i^\nu \partial_l [\mathcal{G}_{jk}^\nu f_0'(\varepsilon_\nu)]$ , so the derivative  $\partial_l \mathcal{G}_{jk}^\nu$  can be written as  $\Gamma_{j,lk}^{(G),\nu} + \Gamma_{k,lj}^{(G),\nu}$ , with  $\Gamma_{c,ab}^{(G),\nu} = \frac{1}{2}(\partial_a \mathcal{G}_{bc}^\nu + \partial_b \mathcal{G}_{ac}^\nu - \partial_c \mathcal{G}_{ab}^\nu)$ . In a two-band model the band-normalized metric is  $\mathcal{G}_{jk}^\nu = 2g_{jk}^\nu/\Delta_{\nu\bar{\nu}}$ , with  $g_{jk}^\nu$  the quantum metric and  $\Delta_{\nu\bar{\nu}}$  the interband gap, so this reorganization extracts the gap-weighted Christoffel structure but leaves an additional gap-gradient term  $-2(\partial_l \Delta_{\nu\bar{\nu}})g_{jk}^\nu/\Delta_{\nu\bar{\nu}}^2$  that vanishes only when the interband gap is momentum independent [48]. The transport contribution is the orbital-moment octupole. In a two-band model, using  $m_i^\nu = (e\Delta_{\nu\bar{\nu}}/2\hbar)\Omega_i^\nu$  with  $\Omega_i^\nu$  the Berry curvature, it becomes a gap-weighted Berry-curvature octupole, reducing to a pure Berry-curvature octupole only when the gap is momentum independent.

*Contribution diagnostics.* Although point-group symmetry cannot separate the three contributions, their dynamical fingerprints can. In the low-frequency single-relaxation-time reduction of Eq. (3), the mixed-quadrupole and metric contributions are both linear in  $\tau$ , whereas the orbital-moment-octupole transport contribution scales as  $\tau^3$  [48]. Their finite-frequency dispersion also differs. For an ordered input sequence  $(j, \omega_1), (k, \omega_2), (l, \omega_3)$ , the mixed-quadrupole contribution relaxes at the last input frequency  $\omega_3$ , the metric contribution at the output frequency  $\Omega = \omega_1 + \omega_2 + \omega_3$ , and the transport contribution at all three of  $\omega_3, \omega_2 + \omega_3$ , and  $\Omega$ . The physical response is obtained by symmetrizing over the paired input labels [48]. For a degenerate THG drive, this corresponds to crossovers at  $\omega\tau \sim 1$  for the mixed quadrupole,  $3\omega\tau \sim 1$  for the metric term, and at  $\omega\tau, 2\omega\tau$ , and  $3\omega\tau \sim 1$  for the transport contribution.

In the dc or quasi-static regime, the Drude factors  $(1 - i\omega_r\tau)^{-1}$  on each leg approach unity, and the scalar  $C_{3v}$  coefficient defined in Eq. (10) reduces to  $\bar{\chi} = A_H\tau + A_G\tau + A_{\text{tr}}\tau^3$ , with  $A_H$ ,  $A_G$ , and  $A_{\text{tr}}$  the lifetime-independent band-geometry amplitudes [48]. A log-log plot of  $|\bar{\chi}|$  versus  $\tau$  therefore crosses from slope 1 in the disorder-dominated geometric regime to slope 3 in the clean transport-dominated regime, unless one of the microscopic coefficients is accidentally suppressed [48]. This lifetime scaling separates the two geometric contributions collectively from the transport contribution, while gate and frequency diagnostics distinguish the mixed quadrupole from the metric term. This separation refers to the clean Ward-complete ker-

nel and can be complicated by extrinsic scattering, since side-jump terms are typically  $\tau$ -independent and could mimic geometric scaling in the moderate-disorder window, while skew-scattering adds process-dependent powers of  $\tau$  [15, 16, 22, 53]. The diagnostic is therefore strongest when combined with the gate-tunable cutoff-independent fingerprint of the metric contribution and with two-color frequency scans. In particular, for the weak-warping two-band  $C_{3v}$  model analyzed below, the metric contribution scales as  $\mu^{-2}$  with the gate-controlled chemical potential, which provides a direct electrostatic test [48]. For  $k_B T \ll |\mu|$  and away from band singularities, the remaining temperature dependence enters mainly through Fermi-surface smearing and  $\tau(T)$ . With an independent calibration of  $\tau(T)$ , temperature or disorder scans can factor out the lifetime powers [54, 55].

*$C_{3v}$  benchmark and lattice completion.* To illustrate the three diagnostics, we use the standard hexagonally warped topological-insulator surface Hamiltonian [28, 48],

$$H_{C_{3v}}(\mathbf{k}) = \left( \frac{k_x^2 + k_y^2}{2m^*} - \mu \right) \sigma_0 + v(k_x \sigma_y - k_y \sigma_x) + \lambda(k_x^3 - 3k_x k_y^2) \sigma_z, \quad (9)$$

where  $m^*$  is the band mass,  $v$  is the Dirac velocity,  $\lambda$  is the hexagonal-warping strength,  $\sigma_0$  is the identity and  $\sigma_{x,y,z}$  are the Pauli matrices, the Fermi level is set to zero, and  $\mu$  is the gate-controlled chemical-potential offset. The cubic warping  $w(\mathbf{k}) = k^3 \cos 3\varphi_{\mathbf{k}}$ , with  $\varphi_{\mathbf{k}}$  the polar angle of  $\mathbf{k}$ , is the lowest-order  $C_{3v}$  anisotropy compatible with time reversal in this surface model [28], and it breaks inversion and supplies the anisotropy needed for the out-of-plane orbital magnetization. For the crystalline orientation in Eq. (9), the  $C_{3v}$  axial rank-four tensor reduces, for in-plane fields, to a single scalar coefficient [38–40, 48],

$$M_z^{(3)} = \bar{\chi} E_0^3 \cos 3\phi, \quad (10)$$

where  $\mathbf{E} = E_0(\cos \phi, \sin \phi, 0)$  and  $\bar{\chi} = \bar{\chi}_H + \bar{\chi}_G + \bar{\chi}_{\text{tr}}$ .

In the weak-warping regime  $|\lambda|k_F^2 \ll v$ , with  $k_F$  the Fermi wavevector, and at zero temperature, the Fermi-surface integral of Eq. (5b) gives

$$\bar{\chi}_G^{T=0} = \frac{e^4 \tau \lambda}{32\pi \hbar^2 \mu^2} + O(\lambda^3), \quad (11)$$

which provides the gate-tunable  $\mu^{-2}$  fingerprint of the metric/Christoffel channel. The continuum model does not determine all remaining coefficients in a cutoff-independent way. The transport coefficient  $\bar{\chi}_{\text{tr}}$  depends on the ultraviolet regularization of the continuum integral, while the mixed-quadrupole coefficient  $\bar{\chi}_H$  requires the interband magnetic matrix element, or equivalently a microscopic magnetic-coupling prescription. In this

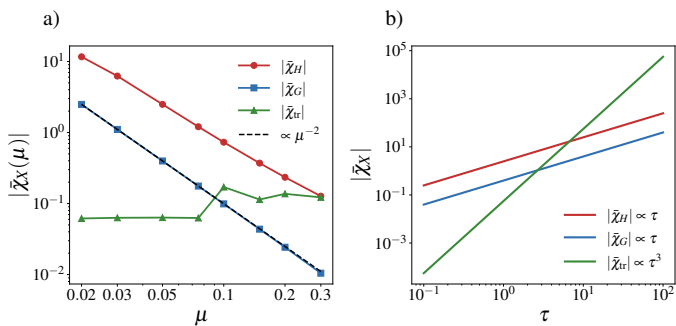


FIG. 2. Contribution-resolved cubic magnetization in the  $C_{3v}$  model of Eq. (9). (a) The three coefficients  $|\bar{\chi}_H|$ ,  $|\bar{\chi}_G|$ , and  $|\bar{\chi}_{tr}|$  as functions of chemical potential  $\mu$ , with the dashed line the  $\mu^{-2}$  prediction of Eq. (11) for  $|\bar{\chi}_G|$ . The ordering of the three magnitudes shown here is not universal and depends on microscopic details of the material. (b) The same coefficients as functions of relaxation time  $\tau$ , showing the  $\tau^1$  scaling of the geometric contributions and the  $\tau^3$  scaling of the transport contribution from Eqs. (5).

sense, the metric channel is the cleanest theoretical prediction of the framework, in that the other two contributions are well-defined gauge-invariant operators but their amplitudes are model-dependent. A triangular-lattice completion of Eq. (9), described in the Supplemental Material, fixes these ultraviolet and magnetic-coupling ambiguities while reproducing the same  $C_{3v}$  Hamiltonian near  $\Gamma$  [48].

Figure 2 confirms the two predicted fingerprints, the gate-tunable  $\mu^{-2}$  law of Eq. (11) for the metric term and the  $\tau^1$  versus  $\tau^3$  separation of the geometric and transport contributions. Their relative magnitudes are not universal and depend on microscopic details of the material.

**THG-MOKE detection and material platforms.** The finite-frequency cubic magnetization can be accessed by third-harmonic magneto-optical Kerr spectroscopy. For a degenerate in-plane drive at frequency  $\omega$ , the emitted magnetization component at  $\Omega = 3\omega$  is

$$M_z^{(3)}(3\omega) = [\bar{\chi}_H + \bar{\chi}_G + \bar{\chi}_{tr}]_{(3\omega, \omega, \omega)} E_0^3 \cos 3\phi$$

in the crystalline convention of Eq. (9). The corresponding Kerr rotation and ellipticity are proportional to the magneto-optical source at  $3\omega$ ,

$$\theta_K(3\omega) + i\eta_K(3\omega) = F(3\omega, n_s, d, \sigma_{\text{opt}}, \dots) M_z^{(3)}(3\omega),$$

where the optical factor  $F$  is fixed by the transfer matrix of the film, substrate, and optical boundary conditions. In the idealized normal-incidence bulk limit this reduces schematically to the familiar estimate  $\theta_K + i\eta_K \simeq (4\pi/c)M_z^{(3)}/(n^2 - 1)$ , with  $c$  the speed of light and  $n$  the refractive index, but quantitative extraction in thin films or surface-state systems should use the full optical geometry [48, 56–58]. This is the cubic analogue of

the SHG-MOKE strategy of Ref. [24]. Using Eq. (11) with  $\lambda \sim 250 \text{ eV \AA}^3$ ,  $\mu \sim 0.1 \text{ eV}$ , and  $\tau \sim 10^{-13} \text{ s}$  gives a sheet response  $|\bar{\chi}_G| \simeq 9.2 \times 10^{-30} \text{ A(V/m)}^{-3}$ . For  $E_0 \sim 10^4 \text{ V cm}^{-1}$  this gives  $M_z^{(3)} \simeq 9.2 \times 10^{-12} \text{ A}$ , equivalent to about  $1.0 \times 10^{-6} \mu_B \text{ nm}^{-2}$  for the metric channel at  $3\omega$ . The corresponding Kerr scale is therefore a demanding small-signal target and should be estimated with the full optical transfer matrix. Since the signal scales as  $E_0^3$ , a stronger pulsed THz drive with  $E_0 \sim 10^5 \text{ V cm}^{-1}$  would enhance the same estimate by  $10^3$  and give  $M_z^{(3)} \sim 10^{-3} \mu_B \text{ nm}^{-2}$ .

THG-MOKE measures a coherent sum of all active cubic contributions rather than a contribution-resolved observable, and even the frequency rolloffs become superposed under a single-color drive. For a degenerate pump the symmetrization over the three input legs averages the ordered  $\omega_3$ ,  $\omega_2 + \omega_3$ , and  $\Omega$  Drude denominators, so the per-contribution rolloffs derived in the Supplemental Material are recovered only in a non-degenerate two-color experiment. A three-way decomposition can nevertheless be obtained by combining the diagnostics derived above. Disorder or temperature scans calibrated by an independent  $\tau$  measurement separate geometric from transport scaling, electrostatic gating tests Eq. (11), and non-degenerate two-color measurements resolve the distinct ordered-kernel rolloffs [48].

Possible backgrounds, including ordinary optical third-harmonic generation, inverse-Faraday effects, drive-induced Oersted fields, and bolometric heating, should be controlled rather than assumed absent. The usual inverse-Faraday source is quadratic in the optical field and vanishes for a linearly polarized drive [59, 60], whereas the cubic magnetization studied here is finite for linear polarization and carries the  $\cos 3\phi$  or  $\sin 3\phi$  angular fingerprint of  $C_{3v}$ . Comparing linear and circular polarizations, together with the  $C_{3v}$  harmonic, phase-sensitive Kerr detection, the cubic power law in the drive field, gate tracking, and two-color frequency dependence, gives discriminants that a substrate-dominated, thermal, or purely optical background is not expected to reproduce simultaneously [48].

The most direct platforms are  $C_{3v}$  topological-insulator surfaces such as  $\text{Bi}_2\text{Se}_3$  and  $\text{Bi}_2\text{Te}_3$ , where hexagonal warping realizes Eq. (9) and surface gating can test Eq. (11) [28, 29]. Hexagonal moiré heterobilayers provide a tunable setting in which twist angle, displacement field, and carrier density can modify both the warping and the active Fermi surfaces, while flat bands may enhance the orbital moment and quantum metric near moiré Dirac points [30–35, 61–63]. Zincblende-type tetrahedral crystals supply a three-dimensional realization of the same cubic-leading axial response [36, 37]. Orthorhombic  $T_d$ -phase  $\text{WTe}_2$  and  $\text{MoTe}_2$  are useful comparison platforms because existing nonlinear Kerr and SHG-MOKE methods can be extended to the  $3\omega$  chan-

nel, even though quadratic magnetization channels are symmetry allowed [23, 24, 64, 65].

*Discussion.* The finite- $q$  Kubo construction developed here is not tied to the  $C_{3v}$  model. For any noncentrosymmetric point group, the antisymmetric  $q$ -linear projection separates the magnetization part of the cubic current response from the uniform transport response. Point-group symmetry determines which components of the resulting axial rank-four tensor are allowed, but it does not distinguish the microscopic origins contained in Eq. (5). Those must be identified dynamically.

Magnetic noncentrosymmetric crystals enlarge this structure. Once time reversal is broken, an additional low-frequency contribution  $\beta^{(\mathcal{M}\delta f)} \equiv \delta m^{(1)}\delta f^{(2)}$  can survive, with  $\delta m^{(1)}$  the linear field-induced correction to the band orbital moment and  $\delta f^{(2)}$  the second-order correction to the distribution function. The contributing band objects are odd under  $\mathbf{k} \rightarrow -\mathbf{k}$  when time reversal is unbroken, so  $\beta^{(\mathcal{M}\delta f)}$  vanishes in nonmagnetic crystals but can be finite in noncentrosymmetric magnets. The resulting symmetry classification of centrosymmetric, time-reversal-symmetric noncentrosymmetric,  $PT$ -symmetric noncentrosymmetric magnetic, and generic noncentrosymmetric magnetic classes is summarized in Table S2 of the Supplemental Material [48]. A particularly useful limiting case is provided by  $PT$ -symmetric noncentrosymmetric magnets. For nondegenerate isolated bands,  $PT$  symmetry enforces  $m_i^\nu = 0$  and removes the mixed-quadrupole moment correction, so the mixed-quadrupole, metric, and transport contributions vanish while  $\beta^{(\mathcal{M}\delta f)}$  may remain. Thus this class can isolate the magnetic contribution, although degenerate  $PT$  bands require the corresponding non-Abelian trace formulation.

The framework admits several extensions. The scaling analysis used a scalar relaxation time inserted after the Ward-complete clean kernel was organized, and quantitative material predictions should add energy-dependent lifetimes, vertex corrections, side-jump, and skew-scattering mechanisms known from nonlinear Hall transport [66–68]. These renormalize the crossover and add extrinsic pieces, but the clean geometric decomposition provides the reference structure. The theory connects naturally to orbitronics, where recent experiments access current-induced orbital magnetization through orbital Hall and orbital Edelstein effects [65, 69–73], the present response being their cubic quantum-geometric counterpart. In correlated metals, the band objects  $H_{ijk}^\nu$ ,  $\mathcal{G}_{jk}^\nu$ , and  $m_i^\nu$  should be replaced by interacting Green-function or quasiparticle analogues, paralleling the interacting theory of equilibrium orbital magnetization [74, 75]. Cubic orbital magnetization therefore probes Bloch-state geometry beyond the Berry-curvature-dipole level.

*Acknowledgments.* This work was supported by the Research Council of Norway through its Centers of Excellence funding scheme, Project No. 353919 and Project

No. 361800 “QTransMag.”

\* tohidfrjpr@gmail.com

- [1] T. Liu, X.-B. Qiang, H.-Z. Lu, and X. C. Xie, Quantum geometry in condensed matter, *Natl. Sci. Rev.* **12**, nwae334 (2024).
- [2] N. Verma, P. J. W. Moll, T. Holder, and R. Queiroz, Quantum geometry and the hidden scales in materials, *Nat. Rev. Phys.* **8**, 226 (2026).
- [3] Y. Jiang, T. Holder, and B. Yan, Revealing quantum geometry in nonlinear quantum materials, *Rep. Prog. Phys.* **88**, 076502 (2025).
- [4] N. Nagaosa and Y. Yanase, Nonreciprocal transport and optical phenomena in quantum materials, *Annu. Rev. Condens. Matter Phys.* **15**, 63 (2024).
- [5] I. Sodemann and L. Fu, Quantum nonlinear Hall effect induced by Berry curvature dipole in time-reversal invariant materials, *Phys. Rev. Lett.* **115**, 216806 (2015).
- [6] Q. Ma, S.-Y. Xu, H. Shen, D. MacNeill, V. Fatemi, T.-R. Chang, A. M. Mier Valdivia, S. Wu, Z. Du, C.-H. Hsu, S. Fang, Q. D. Gibson, K. Watanabe, T. Taniguchi, R. J. Cava, E. Kaxiras, H.-Z. Lu, H. Lin, L. Fu, N. Gedik, and P. Jarillo-Herrero, Observation of the nonlinear Hall effect under time-reversal-symmetric conditions, *Nature* **565**, 337 (2019).
- [7] N. Wang, D. Kaplan, Z. Zhang, T. Holder, N. Cao, A. Wang, X. Zhou, F. Zhou, Z. Jiang, C. Zhang, S. Ru, H. C. Cai, K. Watanabe, T. Taniguchi, B. Yan, and W. Gao, Quantum-metric-induced nonlinear transport in a topological antiferromagnet, *Nature* **621**, 487 (2023).
- [8] A. Gao, Y.-F. Liu, J.-X. Qiu, B. Ghosh, T. V. Trevisan, Y. Onishi, C. Hu, T. Qian, H.-J. Tien, S.-W. Chen, M. Huang, D. Bérubé, H. Li, C. Tzschaschel, T. Dinh, Z. Sun, S.-C. Ho, S.-W. Lien, B. Singh, K. Watanabe, T. Taniguchi, D. C. Bell, H. Lin, T.-R. Chang, C. R. Du, A. Bansil, L. Fu, N. Ni, P. P. Orth, Q. Ma, and S.-Y. Xu, Quantum metric nonlinear Hall effect in a topological antiferromagnetic heterostructure, *Science* **381**, 181 (2023).
- [9] X.-Y. Liu, A.-Q. Wang, R.-Z. Cheng, and Z.-M. Liao, Giant third-order nonlinearity induced by the quantum metric quadrupole in few-layer WTe<sub>2</sub>, *Phys. Rev. Lett.* **134**, 026305 (2025).
- [10] J.-X. Yu, J. Zhao, X. Wang, W. Niu, and Y.-W. Fang, Quantum metric third-order nonlinear Hall effect in a non-centrosymmetric ferromagnet, *Nat. Commun.* **16**, 7698 (2025).
- [11] S. Sankar, R. Liu, C.-P. Zhang, Q.-F. Li, C. Chen, X.-B. Gao, J. Zheng, Y.-H. Lin, K. Qian, R.-H. Yu, X.-C. Zhang, J. Hone, H. C. Po, K. T. Law, X. Du, and A. W. Tsen, Experimental evidence for a Berry curvature quadrupole in an antiferromagnet, *Phys. Rev. X* **14**, 021046 (2024).
- [12] H. Li, C.-P. Zhang, C. Zhou, C. Ma, X. Lei, Z.-Y. Jin, H.-Y. He, B. Li, K. T. Law, and J.-N. Wang, Quantum geometry quadrupole-induced third-order nonlinear transport in antiferromagnetic topological insulator MnBi<sub>2</sub>Te<sub>4</sub>, *Nat. Commun.* **15**, 7779 (2024).
- [13] T. Farajollahpour, R. Ganesh, and K. V. Samokhin, Light-induced charge and spin hall currents in materi-

- als with C4K symmetry, *npj Quantum Materials* **10**, 29 (2025).
- [14] T. Farajollahpour, R. Ganesh, and K. V. Samokhin, Berry curvature-induced transport signature for altermagnetic order, *npj Quantum Materials* **10**, 77 (2025).
- [15] S. Lai, H. Liu, Z. Zhang, J. Zhao, X. Feng, N. Wang, C. Tang, Y. Liu, K. S. Novoselov, S. A. Yang, and W.-b. Gao, Third-order nonlinear Hall effect induced by the Berry-connection polarizability tensor, *Nat. Nanotechnol.* **16**, 869 (2021).
- [16] H. Liu, J. Zhao, Y.-X. Huang, W. Wu, X.-L. Sheng, C. Xiao, and S. A. Yang, Berry connection polarizability tensor and third-order Hall effect, *Phys. Rev. B* **105**, 045118 (2022).
- [17] C.-P. Zhang, X.-J. Gao, Y.-M. Xie, H. C. Po, and K. T. Law, Higher-order nonlinear anomalous Hall effects induced by Berry curvature multipoles, *Phys. Rev. B* **107**, 115142 (2023).
- [18] D. Mandal, S. Sarkar, K. Das, and A. Agarwal, Quantum geometry induced third-order nonlinear transport responses, *Phys. Rev. B* **110**, 195131 (2024).
- [19] Y. Fang, J. Cano, and S. A. A. Ghorashi, Quantum geometry induced nonlinear transport in altermagnets, *Phys. Rev. Lett.* **133**, 106701 (2024).
- [20] R. Y. Chu, L. Han, Z. H. Gong, X. Z. Fu, H. Bai, H.-Z. Lu, and C. Song, Third-order nonlinear Hall effect in altermagnet RuO<sub>2</sub>, *Phys. Rev. Lett.* **135**, 216703 (2025).
- [21] K. Das, S. Lahiri, R. B. Atencia, D. Culcer, and A. Agarwal, Intrinsic nonlinear conductivities induced by the quantum metric, *Phys. Rev. B* **108**, L201405 (2023).
- [22] P. He, H. Isobe, G. K. W. Koon, J. Y. Tan, J. Hu, J. Li, N. Nagaosa, and J. Shen, Third-order nonlinear Hall effect in a quantum Hall system, *Nat. Nanotechnol.* **19**, 1460 (2024).
- [23] X.-B. Qiang, X. Liu, H.-Z. Lu, and X. C. Xie, Quantum Christoffel nonlinear magnetization, *Phys. Rev. Lett.* **136**, 056302 (2026).
- [24] X. Qian, X.-B. Qiang, W. Zhu, Y. Huang, Y. Chen, H.-Z. Lu, Y. Ji, and K. Wang, Probing quantum geometric nonlinear magnetization via second-harmonic magneto-optical Kerr effect, *Phys. Rev. B* **113**, L041407 (2026).
- [25] H. Zhang, C.-X. Liu, X.-L. Qi, X. Dai, Z. Fang, and S.-C. Zhang, Topological insulators in Bi<sub>2</sub>Se<sub>3</sub>, Bi<sub>2</sub>Te<sub>3</sub> and Sb<sub>2</sub>Te<sub>3</sub> with a single Dirac cone on the surface, *Nature Physics* **5**, 438 (2009).
- [26] Y. Xia, D. Qian, D. Hsieh, L. Wray, A. Pal, H. Lin, A. Bansil, D. Grauer, Y. S. Hor, R. J. Cava, and M. Z. Hasan, Observation of a large-gap topological-insulator class with a single Dirac cone on the surface, *Nature Physics* **5**, 398 (2009).
- [27] Y. L. Chen, J. G. Analytis, J.-H. Chu, Z. K. Liu, S.-K. Mo, X. L. Qi, H. J. Zhang, D. H. Lu, X. Dai, Z. Fang, S. C. Zhang, I. R. Fisher, Z.-X. Hussain, and Z.-X. Shen, Experimental realization of a three-dimensional topological insulator, Bi<sub>2</sub>Te<sub>3</sub>, *Science* **325**, 178 (2009).
- [28] L. Fu, Hexagonal warping effects in the surface states of the topological insulator bi<sub>2</sub>te<sub>3</sub>, *Phys. Rev. Lett.* **103**, 266801 (2009).
- [29] D. Hsieh, F. Mahmood, J. W. McIver, D. R. Gardner, Y. S. Lee, and N. Gedik, Nonlinear optical probe of tunable surface electrons on a topological insulator, *Phys. Rev. Lett.* **106**, 057401 (2011).
- [30] F. Wu, T. Lovorn, E. Tutuc, and A. H. MacDonald, Hubbard model physics in transition metal dichalcogenide moiré bands, *Physical Review Letters* **121**, 026402 (2018).
- [31] T. Devakul, V. Crépel, Y. Zhang, and L. Fu, Magic in twisted transition metal dichalcogenide bilayers, *Nature Communications* **12**, 6730 (2021).
- [32] J. Cai, E. Anderson, C. Wang, X. Zhang, X. Liu, W. Holtzmann, Y. Zhang, F. Fan, T. Taniguchi, K. Watanabe, Y. Ran, T. Cao, L. Fu, D. Xiao, W. Yao, and X. Xu, Signatures of fractional quantum anomalous Hall states in twisted MoTe<sub>2</sub>, *Nature* **622**, 63 (2023).
- [33] H. Park, J. Cai, E. Anderson, Y. Zhang, J. Zhu, X. Liu, C. Wang, W. Holtzmann, C. Hu, Z. Liu, T. Taniguchi, K. Watanabe, J.-H. Chu, T. Cao, L. Fu, W. Yao, C.-Z. Chang, D. Cobden, D. Xiao, and X. Xu, Observation of fractionally quantized anomalous Hall effect, *Nature* **622**, 74 (2023).
- [34] Y. Zeng, Z. Xia, K. Kang, J. Zhu, P. Knuppel, C. Vaswani, K. Watanabe, T. Taniguchi, K. F. Mak, and J. Shan, Thermodynamic evidence of fractional Chern insulator in moiré MoTe<sub>2</sub>, *Nature* **622**, 69 (2023).
- [35] F. Xu, Z. Sun, T. Jia, C. Liu, C. Xu, C. Li, Y. Gu, K. Watanabe, T. Taniguchi, B. Tong, J. Jia, Z. Shi, S. Jiang, Y. Zhang, X. Liu, and T. Li, Observation of integer and fractional quantum anomalous Hall effects in twisted bilayer MoTe<sub>2</sub>, *Phys. Rev. X* **13**, 031037 (2023).
- [36] G. Dresselhaus, Spin-orbit coupling effects in zinc blende structures, *Physical Review* **100**, 580 (1955).
- [37] R. Winkler, *Spin-Orbit Coupling Effects in Two-Dimensional Electron and Hole Systems* (Springer, Berlin, 2003).
- [38] G. F. Koster, J. O. Dimmock, R. G. Wheeler, and H. Statz, *Properties of the Thirty-Two Point Groups* (MIT Press, Cambridge, MA, 1963).
- [39] G. L. Bir and G. E. Pikus, *Symmetry and Strain-Induced Effects in Semiconductors* (Wiley, New York, 1974).
- [40] J. F. Nye, *Physical Properties of Crystals, Their Representation by Tensors and Matrices* (Oxford University Press, Oxford, 1985).
- [41] A. A. Soluyanov, D. Gresch, Z. Wang, Q. Wu, M. Troyer, X. Dai, and B. A. Bernevig, Type-II Weyl semimetals, *Nature* **527**, 495 (2015).
- [42] Y. Sun, S.-C. Wu, M. N. Ali, C. Felser, and B. Yan, Prediction of Weyl semimetal in orthorhombic MoTe<sub>2</sub>, *Physical Review B* **92**, 161107 (2015).
- [43] S. Lahiri, K. Das, D. Culcer, and A. Agarwal, Intrinsic nonlinear anomalous Hall effect in  $\mathcal{PT}$ -symmetric antiferromagnets, *Phys. Rev. B* **110**, 195119 (2024).
- [44] C. Xiao, H. Liu, W. Wu, H. Wang, Q. Niu, and S. A. Yang, Time-reversal-even nonlinear current induced by an electric field, *Phys. Rev. Lett.* **130**, 166302 (2023).
- [45] D. Xiao, J. Shi, and Q. Niu, Berry phase correction to electron density of states in solids, *Phys. Rev. Lett.* **95**, 137204 (2005).
- [46] J. Shi, G. Vignale, D. Xiao, and Q. Niu, Quantum theory of orbital magnetization and its generalization to interacting systems, *Phys. Rev. Lett.* **99**, 197202 (2007).
- [47] D. Xiao, M.-C. Chang, and Q. Niu, Berry phase effects on electronic properties, *Rev. Mod. Phys.* **82**, 1959 (2010).
- [48] See Supplemental Material for the minimal-coupling construction of the cubic Kubo kernel with all 26 Ward-identity-completing contact terms, the antisymmetric  $q$ -linear projection to the magnetization tensor, the low-frequency reduction to the three sectors  $\beta^{(H)}$ ,  $\beta^{(G)}$ ,  $\beta^{(tr)}$  with their Drude structures, the closed-form  $C_{3v}$  re-

- sult  $\bar{\chi}_G \propto \mu^{-2}$ , point-group component tables, and the triangular-lattice benchmark.
- [49] C. Aversa and J. E. Sipe, Nonlinear optical susceptibilities of semiconductors, results with a length-gauge analysis, *Phys. Rev. B* **52**, 14636 (1995).
- [50] J. E. Sipe and A. I. Shkrebti, Second-order optical response in semiconductors, *Phys. Rev. B* **61**, 5337 (2000).
- [51] D. E. Parker, T. Morimoto, J. Orenstein, and J. E. Moore, Diagrammatic approach to nonlinear optical response with application to Weyl semimetals, *Phys. Rev. B* **99**, 045121 (2019).
- [52] J. Ahn, G.-Y. Guo, N. Nagaosa, and A. Vishwanath, Riemannian geometry of resonant optical responses, *Nat. Phys.* **18**, 290 (2022).
- [53] Z. Z. Du, H.-Z. Lu, and X. C. Xie, Nonlinear Hall effects, *Nat. Rev. Phys.* **3**, 744 (2021).
- [54] Y. Tian, L. Ye, and X. Jin, Proper scaling of the anomalous hall effect, *Phys. Rev. Lett.* **103**, 087206 (2009).
- [55] Z. Z. Du, C. M. Wang, S. Li, H.-Z. Lu, and X. C. Xie, Disorder-induced nonlinear hall effect with time-reversal symmetry, *Nat. Commun.* **10**, 3047 (2019).
- [56] P. N. Argvres, Theory of the Faraday and Kerr effects in ferromagnetics, *Phys. Rev.* **97**, 334 (1955).
- [57] H. S. Bennett and E. A. Stern, Faraday effect in solids, *Phys. Rev.* **137**, A448 (1965).
- [58] A. K. Zvezdin and V. A. Kotov, *Modern Magnetooptics and Magneto-optical Materials* (Institute of Physics Publishing, Bristol, 1997).
- [59] P. S. Pershan, J. P. van der Ziel, and L. D. Malmstrom, Theoretical discussion of the inverse Faraday effect, Raman scattering, and related phenomena, *Phys. Rev.* **143**, 574 (1966).
- [60] A. V. Kimel, A. Kirilyuk, P. A. Usachev, R. V. Pisarev, A. M. Balbashov, and T. Rasing, Ultrafast non-thermal control of magnetization by instantaneous photomagnetic pulses, *Nature* **435**, 655 (2005).
- [61] P. Törmä, S. Peotta, and B. A. Bernevig, Superconductivity, superfluidity and quantum geometry in twisted multilayer systems, *Nat. Rev. Phys.* **4**, 528 (2022).
- [62] H. Tian, X. Gao, Y. Zhang, S. Che, T. Xu, P. Cheung, K. Watanabe, T. Taniguchi, M. Randeria, F. Zhang, C. N. Lau, and M. W. Bockrath, Evidence for Dirac flat band superconductivity enabled by quantum geometry, *Nature* **614**, 440 (2023).
- [63] M. Tanaka, J. L.-J. Wang, T. H. Dinh, D. Rodan-Legrain, S. Zaman, M. Hays, A. Almanakly, B. Kannan, S. Gustavsson, T. P. Orlando, K. Watanabe, T. Taniguchi, W. D. Oliver, and P. Jarillo-Herrero, Superfluid stiffness of magic-angle twisted bilayer graphene, *Nature* **638**, 99 (2025).
- [64] S. Wu, Z. Fei, Z. Sun, Y. Yi, X. Xu, and S. Wu, Extrinsic nonlinear Kerr rotation in topological materials under a magnetic field, *ACS Nano* **17**, 18158 (2023).
- [65] X.-G. Ye, P.-F. Zhu, W.-Z. Xu, T.-Y. Zhao, and Z.-M. Liao, Nonlinear spin and orbital Edelstein effect in  $\text{WTe}_2$ , *Phys. Rev. B* **110**, L201407 (2024).
- [66] S. Nandy and I. Sodemann, Symmetry and quantum kinetics of the nonlinear Hall effect, *Phys. Rev. B* **100**, 195117 (2019).
- [67] C. Xiao, Z. Z. Du, and Q. Niu, Theory of nonlinear Hall effects, modified semiclassics from quantum kinetics, *Phys. Rev. B* **100**, 165422 (2019).
- [68] Z. Z. Du, C. M. Wang, H.-P. Sun, H.-Z. Lu, and X. C. Xie, Quantum theory of the nonlinear Hall effect, *Nat. Commun.* **12**, 5038 (2021).
- [69] Y.-G. Choi, D. Jo, K.-H. Ko, D. Go, K.-H. Kim, H. G. Park, C. Kim, B.-C. Min, G.-M. Choi, and H.-W. Lee, Observation of the orbital Hall effect in a light metal Ti, *Nature* **619**, 52 (2023).
- [70] I. Lyalin, S. Alikhah, M. Berritta, P. M. Oppeneer, and R. K. Kawakami, Magneto-optical detection of the orbital Hall effect in chromium, *Phys. Rev. Lett.* **131**, 156702 (2023).
- [71] H. Hayashi, D. Go, S. Haku, Y. Mokrousov, and K. Ando, Observation of orbital pumping, *Nat. Electron.* **7**, 646 (2024).
- [72] H. Wang, Y.-X. Huang, H. Liu, X. Feng, J. Zhu, W. Wu, C. Xiao, and S. A. Yang, Orbital origin of the intrinsic planar Hall effect, *Phys. Rev. Lett.* **132**, 056301 (2024).
- [73] D. Go, D. Jo, H.-W. Lee, M. Kläui, and Y. Mokrousov, Orbitorbits, orbital currents in solids, *Europhys. Lett.* **135**, 37001 (2021).
- [74] T. Thonhauser, D. Ceresoli, D. Vanderbilt, and R. Resta, Orbital magnetization in periodic insulators, *Phys. Rev. Lett.* **95**, 137205 (2005).
- [75] D. Ceresoli, T. Thonhauser, D. Vanderbilt, and R. Resta, Orbital magnetization in crystalline solids, multi-band insulators, chern insulators, and metals, *Phys. Rev. B* **74**, 024408 (2006).
- [76] R. Kubo, Statistical-mechanical theory of irreversible processes. i. general theory and simple applications to magnetic and conduction problems, *J. Phys. Soc. Jpn.* **12**, 570 (1957).
- [77] G. D. Mahan, *Many-Particle Physics*, 3rd ed. (Springer, 2000).
- [78] Z. Zhang, X.-Z. Li, and W.-Y. He, Orbital magnetization as the origin of the nonlinear Hall effect, *Phys. Rev. Research* **7**, L042064 (2025).
- [79] Y. Gao, S. A. Yang, and Q. Niu, Field induced positional shift of bloch electrons and its dynamical implications, *Phys. Rev. Lett.* **112**, 166601 (2014).
- [80] G. Sundaram and Q. Niu, Wave-packet dynamics in slowly perturbed crystals, gradient corrections and berry-phase effects, *Phys. Rev. B* **59**, 14915 (1999).
- [81] Y. Gao, S. A. Yang, and Q. Niu, Geometrical effects in orbital magnetic susceptibility, *Phys. Rev. B* **91**, 214405 (2015).
- [82] T. Morimoto, S. Zhong, J. Orenstein, and J. E. Moore, Semiclassical theory of nonlinear magneto-optical responses with applications to topological Dirac/Weyl semimetals, *Phys. Rev. B* **94**, 245121 (2016).
- [83] L. Xiang, C. Zhang, L. Wang, and J. Wang, Third-order intrinsic anomalous Hall effect with generalized semiclassical theory, *Phys. Rev. B* **107**, 075411 (2023).
- [84] J. P. Provost and G. Vall'ee, Riemannian structure on manifolds of quantum states, *Commun. Math. Phys.* **76**, 289 (1980).
- [85] R. Resta, The insulating state of matter, a geometrical theory, *Eur. Phys. J. B* **79**, 121 (2011).
- [86] J. F. Nye, *Physical Properties of Crystals, Their Representation by Tensors and Matrices* (Oxford University Press, 1985).

# Supplemental Material: Three Quantum-Geometric Contributions to Cubic Orbital Magnetization

Tohid Farajollahpour

*Department of Physics, Norwegian University of Science and Technology (NTNU), NO-7491 Trondheim, Norway*  
*Department of Physics, Brock University, St. Catharines, Ontario L2S 3A1, Canada*

In this Supplemental Material, we first construct the clean, noninteracting third-order current kernel from minimal coupling and show how its antisymmetric  $q$ -linear part yields the cubic magnetization. We then derive the gauge-covariant static moment tensor, develop the ordered low-frequency expansion, reduce the diagrammatic kernel to the three dc contributions, summarize the symmetry constraints, and give continuum and lattice models together with experimental diagnostics.

## S1. MINIMAL COUPLING, VERTICES, AND THE FULL THIRD-ORDER KERNEL

The cubic current kernel is built from two standard ingredients: the minimal-coupling prescription for Bloch electrons in an electromagnetic field, and the generating-functional formulation of linear and nonlinear response [51, 76, 77]. Let  $h(\mathbf{k})$  denote the single-particle Bloch Hamiltonian, a matrix in the internal orbital, band, and spin indices, with  $\mathbf{k}$  the crystal momentum. The electromagnetic field enters through a vector potential  $\mathbf{A}(\mathbf{r}, \tau)$ , treated as a classical external source, where  $\mathbf{r}$  is position and  $\tau$  is imaginary (Matsubara) time. In Fourier space its Cartesian components are  $A_a(Q)$ , with  $a \in \{x, y, z\}$  a spatial direction and  $Q \equiv (\mathbf{q}, i\Omega_m)$  a bosonic four-momentum that combines the transferred wavevector  $\mathbf{q}$  with a bosonic Matsubara frequency  $\Omega_m$ . Minimal coupling is the Peierls shift  $\mathbf{k} \rightarrow \mathbf{k} - (e/\hbar)\mathbf{A}$ , in which  $e > 0$  is the elementary charge and  $\hbar$  the reduced Planck constant, so that the field-dressed Bloch Hamiltonian reads

$$h_A(\mathbf{k}) = h\left(\mathbf{k} - \frac{e}{\hbar}\mathbf{A}\right). \quad (\text{S1})$$

In Eq. (S1) the bare symbol  $\mathbf{A}$  is a uniform-field shorthand for the general source  $A_a(Q)$ , whose four-momentum dependence is reinstated when the vertices are assigned incoming momenta below. The single-particle inverse Green function is

$$G^{-1}(K, A) = i\nu_n + \mu - h_A(\mathbf{k}), \quad K \equiv (\mathbf{k}, i\nu_n), \quad (\text{S2})$$

where  $\mu$  is the chemical potential and  $\nu_n$  is a fermionic Matsubara frequency. The grand-potential functional is

$$W[A] = -T \text{Tr} \ln[-G^{-1}(A)], \quad (\text{S3})$$

where  $T$  denotes temperature in energy units. Equation (S3) generates the current-response functions. With the convention

$$j_a(Q) \equiv -\frac{1}{V} \frac{\delta W[A]}{\delta A_a(-Q)}, \quad (\text{S4})$$

variation of Eq. (S3) gives

$$\delta W[A] = -T \text{Tr}[G[A] \delta G^{-1}[A]]. \quad (\text{S5})$$

Therefore the current density can be written as

$$j_a(Q) = \frac{T}{V} \text{Tr}[G[A] X_a(Q, A)], \quad X_a(Q, A) = \frac{\delta G^{-1}[A]}{\delta A_a(-Q)}. \quad (\text{S6})$$

where  $V$  is the crystal volume and  $\text{Tr}$  runs over momentum, fermionic Matsubara frequency, and internal orbital, band, and spin indices. The source vertex  $X_a(Q, A)$  is the functional derivative of  $G^{-1}$  with respect to  $A_a(-Q)$ . At  $A = 0$  it reduces to the usual paramagnetic current vertex  $\Gamma_a^{(1)} = (e/\hbar)\partial_a h$ . Higher derivatives generate the diamagnetic/contact vertices required by nonlinear Ward identities [49, 51]. The higher functional derivatives of  $G^{-1}$  with respect to the source field define the contact (diamagnetic) vertices are given by

$$X_{ab} = \frac{\delta^2 G^{-1}}{\delta A_a \delta A_b}, \quad X_{abc} = \frac{\delta^3 G^{-1}}{\delta A_a \delta A_b \delta A_c}, \quad X_{abcd} = \frac{\delta^4 G^{-1}}{\delta A_a \delta A_b \delta A_c \delta A_d}. \quad (\text{S7})$$

Throughout this section,  $a, j, k, l \in \{x, y, z\}$  denote Cartesian directions and  $\partial_i \equiv \partial/\partial k_i$ . At  $A = 0$  these become the current vertices

$$\Gamma_i^{(1)} = X_i|_{A=0} = \frac{e}{\hbar} \partial_i h, \quad (\text{S8})$$

$$\Gamma_{ij}^{(2)} = X_{ij}|_{A=0} = -\frac{e^2}{\hbar^2} \partial_i \partial_j h, \quad (\text{S9})$$

$$\Gamma_{ijk}^{(3)} = X_{ijk}|_{A=0} = \frac{e^3}{\hbar^3} \partial_i \partial_j \partial_k h, \quad (\text{S10})$$

$$\Gamma_{ijkl}^{(4)} = X_{ijkl}|_{A=0} = -\frac{e^4}{\hbar^4} \partial_i \partial_j \partial_k \partial_l h. \quad (\text{S11})$$

Using  $\delta G = -G(\delta G^{-1})G$ , one finds the first and second functional derivatives. For compactness we write  $\delta_j \equiv \delta/\delta A_j(-Q_1)$ ,  $\delta_k \equiv \delta/\delta A_k(-Q_2)$ , and  $\delta_l \equiv \delta/\delta A_l(-Q_3)$

$$\delta_j j_a = \frac{T}{V} \text{Tr} [-GX_j GX_a + GX_{ja}], \quad (\text{S12})$$

$$\delta_k \delta_j j_a = \frac{T}{V} \text{Tr} \left[ GX_k GX_j GX_a + GX_j GX_k GX_a - GX_{jk} GX_a - GX_j GX_{ka} - GX_k GX_{ja} + GX_{jka} \right]. \quad (\text{S13})$$

Differentiating once more with respect to  $A_l$  yields the exact ordered cubic kernel in compact operator form,

$$\delta_l \delta_k \delta_j j_a = \frac{T}{V} \text{Tr} [\mathcal{B}_{a,jkl} + \mathcal{C}_{a,jkl} + \mathcal{D}_{a,jkl} + \mathcal{Q}_{a,jkl}], \quad (\text{S14})$$

The cubic kernel in Eq. (S14) is an ordered response, with the three incoming fields carrying the ordered label-frequency pairs  $(j, Q_1)$ ,  $(k, Q_2)$ , and  $(l, Q_3)$ . The same ordering convention applies to the cubic magnetization kernel  $\tilde{\beta}_{ijkl}(\Omega, \omega_1, \omega_2, \omega_3)$  introduced below, where  $\Omega = \omega_1 + \omega_2 + \omega_3$  is the output frequency. The physical tensor that enters the symmetry analysis follows from symmetrizing over simultaneous permutations of these three field-index/frequency pairs. Writing  $(j_1, j_2, j_3) \equiv (j, k, l)$ ,

$$\beta_{ijkl}^{\text{phys}}(\Omega, \omega_1, \omega_2, \omega_3) = \frac{1}{3!} \sum_{\pi \in S_3} \tilde{\beta}_{ij_{\pi_1} j_{\pi_2} j_{\pi_3}}(\Omega, \omega_{\pi_1}, \omega_{\pi_2}, \omega_{\pi_3}). \quad (\text{S15})$$

In the static or fully degenerate limit this reduces to ordinary symmetrization over the last three Cartesian indices, the convention adopted in the point-group component tables. For nondegenerate frequency mixing the intrinsic permutation symmetry instead acts on the paired labels  $(j, \omega_1)$ ,  $(k, \omega_2)$ , and  $(l, \omega_3)$ . Equivalently, one may retain the ordered kernels  $\tilde{\beta}$  and sum those ordered contributions that share the same output frequency  $\Omega$ ; Eq. (S15) is the convention in which this sum is absorbed into  $\beta^{\text{phys}}$ .

The four vertex classes entering Eq. (S14) are

$$\mathcal{B}_{a,jkl} = - \sum_{\pi \in S_3} GX_{\pi_3} GX_{\pi_2} GX_{\pi_1} GX_a, \quad (\text{S16})$$

$$\begin{aligned} \mathcal{C}_{a,jkl} = & (GX_{jk} GX_l GX_a + GX_l GX_{jk} GX_a + GX_{jl} GX_k GX_a) \\ & + (GX_k GX_{jl} GX_a + GX_{kl} GX_j GX_a + GX_j GX_{kl} GX_a) \\ & + (GX_j GX_k GX_{al} + GX_k GX_j GX_{al} + GX_j GX_l GX_{ak}) \\ & + (GX_l GX_j GX_{ak} + GX_k GX_l GX_{aj} + GX_l GX_k GX_{aj}), \end{aligned} \quad (\text{S17})$$

$$\begin{aligned} \mathcal{D}_{a,jkl} = & -(GX_{jk} GX_{al} + GX_{jl} GX_{ak} + GX_{kl} GX_{aj}) \\ & - (GX_{jk} GX_a + GX_j GX_{akl} + GX_k GX_{ajl} + GX_l GX_{ajk}), \end{aligned} \quad (\text{S18})$$

$$\mathcal{Q}_{a,jkl} = GX_{ajkl}. \quad (\text{S19})$$

Here  $S_3$  permutes the three incoming labels  $(j, k, l)$  in the box class. The Ward-complete cubic kernel contains  $6 + 12 + 3 + 4 + 1 = 26$  terms. They consist of 6 box terms with four rank-one vertices, 12 mixed-contact terms with one  $\Gamma^{(2)}$ , 3 double-contact terms, 4 cubic-contact terms, and 1 quartic-contact term. The detailed list in Eqs. (S16)

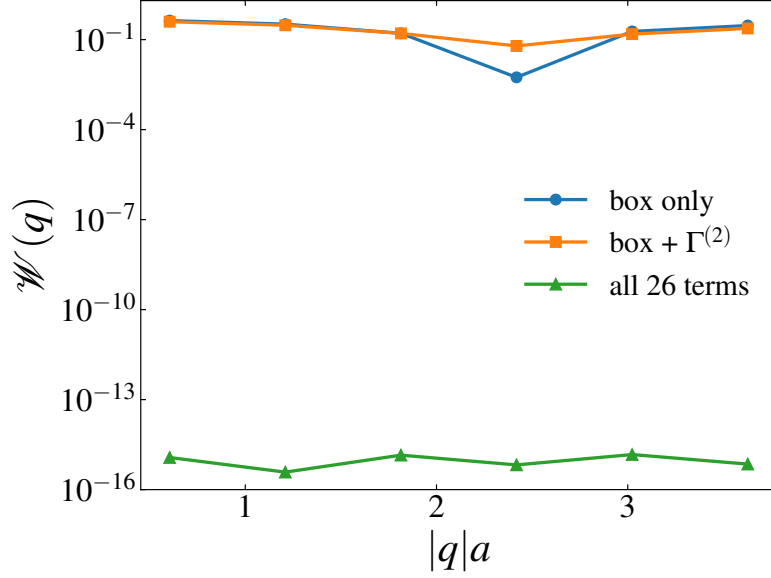


FIG. S1. Output-leg Ward-identity check for the cubic current kernel. We plot the normalized longitudinal residual  $\mathcal{W}(q) = |q_a \tilde{K}_{a,jkl}(q)| / (|q| K_{\text{box}}^{\text{max}})$  for the triangular-lattice Peierls regularization of the  $C_{3v}$  model, with  $K_{\text{box}}^{\text{max}} = \max_a |\tilde{K}_{a,jkl}^{\text{box}}|$ . Parameters are  $a = e = \hbar = v = m^* = 1$ ,  $\lambda = 0.25$ ,  $\mu = 0.15$ ,  $T = 0.25$ , an  $L = 12$  triangular cluster, and 40 positive and negative fermionic Matsubara frequencies. The momenta are  $\mathbf{q}_1 = (n_q/L)\mathbf{b}_1$ ,  $\mathbf{q}_2 = \mathbf{q}_3 = 0$ , and  $\mathbf{q}_0 = -\mathbf{q}_1$ , with ordered polarizations  $(x, y, x)$ . Including the full set of  $6 + 12 + 3 + 4 + 1 = 26$  terms with the finite- $q$  Peierls vertex factors of Eq. (S22) cancels the residual to numerical roundoff, confirming that contact terms are required before the  $q$ -linear magnetization projection.

through (S19) is kept because these contact vertices are not optional. They are generated by differentiating the minimally coupled  $G^{-1}(A)$  and are required by the nonlinear Ward identities. This is the nonlinear analogue of the gauge-invariant organization familiar from optical-response theory [49, 51]. A useful algebraic check is obtained by differentiating the gauge invariance of the source functional,  $W[A + \nabla\chi] = W[A]$ . In four-vector notation the clean full kernel obeys

$$Q_\mu \tilde{K}^{\mu,jkl}(Q, Q_1, Q_2, Q_3) = 0, \quad (\text{S20})$$

with analogous Ward identities on the three incoming legs. In the static long-wavelength limit this reduces to the requirement that a spatially uniform vector potential, which is a pure gauge on a simply connected sample, cannot produce a physical current. The same cancellation can be traced term by term from the vertex identities generated by the Peierls substitution, e.g.,

$$q_a \Gamma_a^{(1)}(\mathbf{k}, \mathbf{q}) = \frac{e}{\hbar} [h(\mathbf{k} + \mathbf{q}) - h(\mathbf{k})] + \mathcal{O}(q^2), \quad (\text{S21})$$

whose next derivatives produce the longitudinal parts of  $\Gamma^{(2)}$ ,  $\Gamma^{(3)}$ , and  $\Gamma^{(4)}$ . The box class alone leaves uncanceled longitudinal pieces, the mixed-, double-, cubic-, and quartic-contact families cancel them so that Eq. (S20) holds before any low-frequency or relaxation-time reduction is made.

The compact vertices in Eqs. (S8) through (S11) are the uniform-field limits of their finite-momentum counterparts. In a Peierls lattice regularization the wavevector also enters the vertices directly. For a hopping matrix  $T_{\mathbf{d}}$  on a straight bond from  $\mathbf{R}$  to  $\mathbf{R} + \mathbf{d}$ , a source leg with wavevector  $\mathbf{q}_r$  and polarization  $\mathbf{e}_r$  contributes the line integral

$$\Phi_r(\mathbf{R}, \mathbf{d}) = (\mathbf{e}_r \cdot \mathbf{d}) \exp \left[ i \mathbf{q}_r \cdot \left( \mathbf{R} + \frac{\mathbf{d}}{2} \right) \right] \text{sinc} \left( \frac{\mathbf{q}_r \cdot \mathbf{d}}{2} \right), \quad \text{sinc } x \equiv \frac{\sin x}{x}. \quad (\text{S22})$$

The  $n$ -leg Peierls vertex follows from the product of the  $n$  corresponding line-integral factors and the Peierls phase differentiated to order  $n$ . At finite lattice spacing the  $q$  derivative in the magnetization projection then acts on both the propagator routing and these vertex form factors, so the Ward-complete kernel retains both contributions. Figure S1 gives a numerical version of the Ward-identity cancellation in Eq. (S20). Incomplete kernels contain spurious longitudinal pieces, whereas the full 26-term kernel is transverse within numerical precision.

Setting  $A = 0$ , replacing  $X \rightarrow \Gamma$ , and assigning the external bosonic four-momenta  $Q_r \equiv (\mathbf{q}_r, i\omega_{rm})$  to the three incoming fields gives the ordered Matsubara kernel, with  $Q = Q_1 + Q_2 + Q_3$  and  $\beta_T \equiv 1/T$

$$\tilde{K}_{a,jkl}(Q, Q_1, Q_2, Q_3) = \frac{1}{\beta_T V} \sum_K \text{Tr} \left[ \tilde{\mathcal{B}}_{a,jkl}(K) + \tilde{\mathcal{C}}_{a,jkl}(K) + \tilde{\mathcal{D}}_{a,jkl}(K) + \tilde{\mathcal{Q}}_{a,jkl}(K) \right]. \quad (\text{S23})$$

The objects  $\tilde{\mathcal{B}}$ ,  $\tilde{\mathcal{C}}$ ,  $\tilde{\mathcal{D}}$ , and  $\tilde{\mathcal{Q}}$  are the momentum-space versions of Eqs. (S16) through (S19) after the replacement  $X \rightarrow \Gamma$ , with the internal Green-function arguments determined by momentum conservation along the matter loop. Defining the partial sums  $P_0 \equiv 0$ ,  $P_1 \equiv Q_{\pi_1}$ ,  $P_2 \equiv Q_{\pi_1} + Q_{\pi_2}$ ,  $P_3 \equiv Q_1 + Q_2 + Q_3 = Q$ , the explicit forms read

$$\tilde{\mathcal{B}}_{a,jkl}(K) = - \sum_{\pi \in S_3} G_{K+P_3} \Gamma_{\pi_3}^{(1)} G_{K+P_2} \Gamma_{\pi_2}^{(1)} G_{K+P_1} \Gamma_{\pi_1}^{(1)} G_K \Gamma_a^{(1)}, \quad (\text{S24})$$

$$\begin{aligned} \tilde{\mathcal{C}}_{a,jkl}(K) = & \left( G_{K+Q} \Gamma_{jk}^{(2)} G_{K+Q_3} \Gamma_l^{(1)} G_K \Gamma_a^{(1)} + G_{K+Q} \Gamma_l^{(1)} G_{K+Q_1+Q_2} \Gamma_{jk}^{(2)} G_K \Gamma_a^{(1)} \right. \\ & + G_{K+Q} \Gamma_{jl}^{(2)} G_{K+Q_2} \Gamma_k^{(1)} G_K \Gamma_a^{(1)} + G_{K+Q} \Gamma_k^{(1)} G_{K+Q_1+Q_3} \Gamma_{jl}^{(2)} G_K \Gamma_a^{(1)} \\ & + G_{K+Q} \Gamma_{kl}^{(2)} G_{K+Q_1} \Gamma_j^{(1)} G_K \Gamma_a^{(1)} + G_{K+Q} \Gamma_j^{(1)} G_{K+Q_2+Q_3} \Gamma_{kl}^{(2)} G_K \Gamma_a^{(1)} \left. \right) \\ & + \left( G_{K+Q} \Gamma_j^{(1)} G_{K+Q_2+Q_3} \Gamma_k^{(1)} G_K \Gamma_{al}^{(2)} + G_{K+Q} \Gamma_k^{(1)} G_{K+Q_1+Q_3} \Gamma_j^{(1)} G_K \Gamma_{al}^{(2)} \right. \\ & + G_{K+Q} \Gamma_j^{(1)} G_{K+Q_2+Q_3} \Gamma_l^{(1)} G_K \Gamma_{ak}^{(2)} + G_{K+Q} \Gamma_l^{(1)} G_{K+Q_1+Q_2} \Gamma_j^{(1)} G_K \Gamma_{ak}^{(2)} \\ & \left. + G_{K+Q} \Gamma_k^{(1)} G_{K+Q_1+Q_3} \Gamma_l^{(1)} G_K \Gamma_{aj}^{(2)} + G_{K+Q} \Gamma_l^{(1)} G_{K+Q_1+Q_2} \Gamma_k^{(1)} G_K \Gamma_{aj}^{(2)} \right), \quad (\text{S25}) \end{aligned}$$

$$\begin{aligned} \tilde{\mathcal{D}}_{a,jkl}(K) = & - \left( G_{K+Q} \Gamma_{jk}^{(2)} G_K \Gamma_{al}^{(2)} + G_{K+Q} \Gamma_{jl}^{(2)} G_K \Gamma_{ak}^{(2)} + G_{K+Q} \Gamma_{kl}^{(2)} G_K \Gamma_{aj}^{(2)} \right) \\ & - \left( G_{K+Q} \Gamma_{jkl}^{(3)} G_K \Gamma_a^{(1)} + G_{K+Q} \Gamma_j^{(1)} G_K \Gamma_{akl}^{(3)} \right. \\ & \left. + G_{K+Q} \Gamma_k^{(1)} G_K \Gamma_{ajl}^{(3)} + G_{K+Q} \Gamma_l^{(1)} G_K \Gamma_{ajk}^{(3)} \right), \quad (\text{S26}) \end{aligned}$$

$$\tilde{\mathcal{Q}}_{a,jkl}(K) = G_K \Gamma_{ajkl}^{(4)}. \quad (\text{S27})$$

The momentum routings follow from the convention that  $A_a(-Q)$  enters the response-leg vertex and from momentum conservation at every vertex. Thus each term in Eqs. (S24) through (S27) is obtained by replacing the operator sequence in Eqs. (S16) through (S19) by the corresponding partial sums of the incoming four-momenta along the loop.

## S2. RETARDED KERNEL AND PRACTICAL $q \rightarrow 0$ EXTRACTION

The ordered Matsubara kernel in Eq. (S23) is continued to the ordered retarded response only after the causal ordering of the paired input labels is fixed. For the ordering  $(j, \omega_1), (k, \omega_2), (l, \omega_3)$  used below, the intraband denominators depend on the tail frequency sums. The fully retarded branch is represented by

$$i\omega_{3m} \rightarrow \omega_3 + i0^+, \quad i(\omega_{2m} + \omega_{3m}) \rightarrow \omega_2 + \omega_3 + i0^+, \quad i\Omega_m \rightarrow \Omega + i0^+. \quad (\text{S28})$$

Here  $\Omega_m = \omega_{1m} + \omega_{2m} + \omega_{3m}$  and  $\Omega = \omega_1 + \omega_2 + \omega_3$ . This is the nested commutator, or equivalently Keldysh, causal branch for the chosen ordered labels. It should not be read as three independent leg continuations. Other causal branches are obtained by permuting the paired labels before applying the same rule and then using the symmetrization of Eq. (S15).

To extract the cubic magnetization tensor we use the fact that the bound (magnetization) part of the current is related to the magnetization density  $M_c$  by Ampère's law,  $\mathbf{j}^{(M)} = \nabla \times \mathbf{M}$ , which in Fourier space at small  $\mathbf{q}$  reads

$$j_a^{(M)}(\mathbf{q}) = i \epsilon_{abc} q_b M_c(\mathbf{q}) + \mathcal{O}(q^2). \quad (\text{S29})$$

Antisymmetrizing in the pair  $(a, b)$  (factor 2) and using the curl identity  $\epsilon_{cab} \epsilon_{abd} = 2\delta_{cd}$  (another factor 2) inverts Eq. (S29),

$$M_c(\mathbf{q} = 0) = \frac{1}{4i} \epsilon_{cab} \left[ \frac{\partial j_a^{(M)}}{\partial q_b} - \frac{\partial j_b^{(M)}}{\partial q_a} \right]_{\mathbf{q}=0}. \quad (\text{S30})$$

This identifies the magnetization with the antisymmetric,  $q$ -linear part of the current, as in the modern theory of orbital magnetization [46, 47, 74, 75]. To convert from the vector-potential kernel  $\tilde{K}_{a,jkl}^R$ , which couples to  $A_j A_k A_l$ , to a kernel that couples to  $E_j E_k E_l$ , we use  $\mathbf{E}_r = -\partial_t \mathbf{A}_r$ , i.e.  $E_r(Q_r) = i\omega_r A_r(Q_r)$  at  $\mathbf{q}_r = 0$ . Hence

$$j_a^{(3)}(Q) = \tilde{K}_{a,jkl}^R(Q, Q_1, Q_2, Q_3) A_j A_k A_l = \frac{\tilde{K}_{a,jkl}^R}{(i\omega_1)(i\omega_2)(i\omega_3)} E_j E_k E_l = \frac{i \tilde{K}_{a,jkl}^R}{\omega_1 \omega_2 \omega_3} E_j E_k E_l. \quad (\text{S31})$$

Identifying the magnetization-current part of  $j_a^{(3)}$  in Eq. (S30) and writing  $M_c = \tilde{\beta}_{c jkl} E_j E_k E_l$  then gives the cubic magnetization-tensor formula

$$\tilde{\beta}_{c jkl}(\Omega, \omega_1, \omega_2, \omega_3) = \frac{1}{4i} \epsilon_{cab} \left[ \frac{\partial}{\partial q_b} \frac{i \tilde{K}_{a,jkl}^R}{\omega_1 \omega_2 \omega_3} - \frac{\partial}{\partial q_a} \frac{i \tilde{K}_{b,jkl}^R}{\omega_1 \omega_2 \omega_3} \right]_{\mathbf{q}=0} = \frac{1}{4\omega_1 \omega_2 \omega_3} \epsilon_{cab} \left[ \frac{\partial \tilde{K}_{a,jkl}^R}{\partial q_b} - \frac{\partial \tilde{K}_{b,jkl}^R}{\partial q_a} \right]_{\mathbf{q}=0}, \quad (\text{S32})$$

where  $\epsilon_{cab}$  is the Levi-Civita symbol and the derivative is taken with respect to the total output wavevector  $\mathbf{q}$  at  $\mathbf{q} = 0$ . The prefactor  $1/4$  combines the factor of two from antisymmetrizing in  $(a, b)$  with the factor of two from the curl identity, the factor  $1/(\omega_1 \omega_2 \omega_3)$  converts the vector-potential kernel to the electric-field kernel through Eq. (S31). The antisymmetric  $q$ -linear projection isolates the magnetization-current part of the response, consistent with modern orbital-magnetization formulations and recent links between nonequilibrium orbital magnetization and nonlinear Hall transport [46, 47, 78].

The ordered tensor in Eq. (S32) follows the convention fixed in Eq. (S15), the point-group tables below use  $\beta^{\text{phys}}$ .

The derivative in Eq. (S32) should be understood with momentum conservation enforced. In a translationally invariant kernel the four external momenta satisfy  $Q_0 + Q_1 + Q_2 + Q_3 = 0$ , where  $Q_0$  is the source momentum on the measured current leg. The small vector  $\mathbf{q}$  can therefore be routed through any one of the incoming fields, distributed among the three incoming fields as a slow envelope momentum of the product  $E_j E_k E_l$ , or equivalently introduced as a magnetic probe coupled to the composite current response. These prescriptions are equivalent in the  $q \rightarrow 0$  antisymmetric projection after the Ward identities are imposed. In the finite-difference notation below,  $\tilde{K}_{a,jkl}^R(q\hat{\mathbf{b}})$  is a shorthand for this momentum-conserving long-wavelength limit, for example  $\mathbf{q}_1 = q\hat{\mathbf{b}}$ ,  $\mathbf{q}_2 = \mathbf{q}_3 = 0$ , and  $\mathbf{q}_0 = -\mathbf{q}_1$ , followed by the input-leg symmetrization of Eq. (S15) when the physical tensor is desired. Approximating the derivatives in Eq. (S32) by symmetric finite differences along  $\hat{\mathbf{a}}$  and  $\hat{\mathbf{b}}$  gives

$$\tilde{\beta}_{c jkl} = \frac{1}{4\omega_1 \omega_2 \omega_3} \epsilon_{cab} \lim_{q \rightarrow 0} \frac{\tilde{K}_{a,jkl}^R(q\hat{\mathbf{b}}) - \tilde{K}_{a,jkl}^R(-q\hat{\mathbf{b}}) - \tilde{K}_{b,jkl}^R(q\hat{\mathbf{a}}) + \tilde{K}_{b,jkl}^R(-q\hat{\mathbf{a}})}{2q}. \quad (\text{S33})$$

Here  $\hat{\mathbf{a}}$  and  $\hat{\mathbf{b}}$  are unit vectors along the Cartesian  $a$  and  $b$  directions. Only the magnitude  $q \rightarrow 0$  enters the limit, and the four kernel evaluations along  $\pm\hat{\mathbf{a}}$  and  $\pm\hat{\mathbf{b}}$  implement the antisymmetric  $q$ -linear projection in Eq. (S30). Dropping contact terms can spoil the Ward-identity cancellations and introduce spurious gauge or routing dependence in the extracted magnetization, as in incomplete gauge-invariant reorganizations of nonlinear optical responses [49, 51].

### S3. GAUGE-COINVARIANT DERIVATION OF THE STATIC CUBIC MOMENT TENSOR

We construct the static second-order correction to the orbital moment in a gauge-covariant form, starting from the mixed electric-magnetic component of the second-order positional-shift functional [79] and following the semi-classical treatment of wave-packet geometry, orbital magnetization, and field-corrected band energies [46, 47, 80, 81]. Throughout,  $\mu, \nu, \eta$  are band indices,  $i, j, k, \alpha, \beta, \gamma$  are Cartesian directions, and  $H \equiv h(\mathbf{k})$  is the Bloch Hamiltonian with cell-periodic eigenstates  $|\mu\rangle \equiv |u_\mu(\mathbf{k})\rangle$  obeying  $h(\mathbf{k})|u_\mu\rangle = \varepsilon_\mu |u_\mu\rangle$  and  $\langle u_\mu | u_\nu \rangle = \delta_{\mu\nu}$ , where  $\varepsilon_\mu(\mathbf{k})$  is the band energy. Define the first-order interband mixing amplitudes

$$R_{\mu\nu}^j(\mathbf{k}) = \frac{A_{\mu\nu}^j(\mathbf{k})}{\Delta_{\nu\mu}} = i \frac{\langle \mu | \partial_j H | \nu \rangle}{\Delta_{\nu\mu}^2}, \quad C_{\mu\nu}^k(\mathbf{k}) = -\frac{m_{\mu\nu}^k(\mathbf{k})}{\Delta_{\nu\mu}(\mathbf{k})}, \quad (\text{S34})$$

where  $A_{\mu\nu}^j = \langle \mu | i\partial_j | \nu \rangle$  is the interband Berry connection,  $\Delta_{\nu\mu} = \varepsilon_\nu - \varepsilon_\mu$  the band-energy difference, and  $m_{\mu\nu}^k$  the interband orbital-moment matrix element. The derivatives  $\partial_j$  act on the cell-periodic states in a smooth gauge, so that  $\langle \mu | \partial_j H | \nu \rangle = -i\Delta_{\nu\mu} A_{\mu\nu}^j$  for  $\mu \neq \nu$ , which gives the second equality in Eq. (S34). The orbital-moment matrix element is the off-diagonal generalization of the single-band moment [46, 47, 74, 75, 80],

$$m_{\mu\nu}^k(\mathbf{k}) = \frac{ie}{2\hbar} \epsilon_{kab} \langle \partial_a u_\mu | [h(\mathbf{k}) - \frac{1}{2}(\varepsilon_\mu + \varepsilon_\nu)] | \partial_b u_\nu \rangle,$$

with  $\epsilon_{kab}$  the Levi-Civita symbol; for  $\mu = \nu$  it reduces to the self-rotation moment  $m_k^{\nu\nu} \equiv m_k^\nu$ . The gauge-covariant derivative of an interband object  $\mathcal{Y}_{\mu\nu}$  is

$$D_\alpha^{\mu\nu} \mathcal{Y}_{\mu\nu} = (A_\alpha^\nu - A_\alpha^\mu - i\partial_\alpha) \mathcal{Y}_{\mu\nu}, \quad (\text{S35})$$

with  $A_\alpha^\mu = \langle \mu | i\partial_\alpha | \mu \rangle$  the intraband Berry connection; under  $|\mu\rangle \rightarrow e^{i\varphi_\mu} |\mu\rangle$  the connection terms cancel the phase gradient of  $\partial_\alpha \mathcal{Y}_{\mu\nu}$ , so that  $D_\alpha^{\mu\nu} \mathcal{Y}_{\mu\nu} \rightarrow e^{i(\varphi_\nu - \varphi_\mu)} D_\alpha^{\mu\nu} \mathcal{Y}_{\mu\nu}$ . This is the length-gauge generalized derivative of Aversa and Sipe [49–51] adapted to the positional-shift formalism [79, 81].

For generic interband amplitudes  $\mathcal{X}$  and  $\mathcal{Y}$ , each standing for either  $R$  or  $C$  of Eq. (S34), define the two bilinear blocks

$$U_{\alpha\beta\gamma}^{\nu\mu}[\mathcal{X}, \mathcal{Y}] = \mathcal{X}_{\nu\mu}^\beta D_\alpha^{\mu\nu} \mathcal{Y}_{\mu\nu}^\gamma, \quad (\text{S36})$$

$$V_{\alpha\beta\gamma}^{\nu\mu\eta}[\mathcal{X}, \mathcal{Y}] = (2\mathcal{X}_{\nu\mu}^\alpha A_{\mu\eta}^\beta + \mathcal{X}_{\nu\mu}^\beta A_{\mu\eta}^\alpha) \mathcal{Y}_{\eta\nu}^\gamma, \quad (\text{S37})$$

which appear after the second-order positional shift is reorganized covariantly. The  $U$  block carries the covariant derivative of a two-band amplitude, and the  $V$  block carries a genuine intermediate-band insertion summed over  $\eta \neq \mu, \nu$ . The asymmetric coefficient (2, 1) in Eq. (S37) is fixed by the pure-electric limit. Setting  $\mathcal{X} = \mathcal{Y} = R$ ,

$$V_{\alpha\beta\gamma}^{\nu\mu\eta}[R, R] = (2R_{\nu\mu}^\alpha A_{\mu\eta}^\beta + R_{\nu\mu}^\beta A_{\mu\eta}^\alpha) R_{\eta\nu}^\gamma, \quad (\text{S38})$$

and substitution into Eq. (S40) reproduces the Gao-Yang-Niu positional shift only when the coefficient of  $R_{\nu\mu}^\alpha A_{\mu\eta}^\beta R_{\eta\nu}^\gamma$  is twice that of  $R_{\nu\mu}^\beta A_{\mu\eta}^\alpha R_{\eta\nu}^\gamma$ , that is

$$c_{\alpha\beta} = 2, \quad c_{\beta\alpha} = 1. \quad (\text{S39})$$

The second-order positional-shift functional is quadratic in the first-order amplitudes and, in covariant form, reduces to the blocks of Eqs. (S36) and (S37). For a generic covariant amplitude  $Z$  (again  $R$  or  $C$ ), with both block arguments set equal,

$$T_{\alpha\beta\gamma}^\nu[Z] = \text{Re} \sum_{\mu \neq \nu} \left[ U_{\alpha\beta\gamma}^{\nu\mu}[Z, Z] + U_{\beta\alpha\gamma}^{\nu\mu}[Z, Z] - U_{\beta\gamma\alpha}^{\nu\mu}[Z, Z] - \sum_{\eta \neq \mu, \nu} V_{\alpha\beta\gamma}^{\nu\mu\eta}[Z, Z] \right]. \quad (\text{S40})$$

The first two  $U$  terms symmetrize  $(\alpha, \beta)$ , and the remaining  $U$  and  $V$  terms reproduce the pure-electric positional shift when  $Z = R$ . To isolate the mixed electric-magnetic part, set  $Z = sR + tC$  with bookkeeping parameters  $s, t$ . Since every block is bilinear,

$$T_{\alpha\beta\gamma}^\nu[sR + tC] = s^2 T_{\alpha\beta\gamma}^\nu[R] + t^2 T_{\alpha\beta\gamma}^\nu[C] + st \mathcal{Q}_{\alpha\beta\gamma}^\nu, \quad (\text{S41})$$

and  $\partial_s \partial_t$  at  $s = t = 0$  selects the two ordered cross terms,

$$\begin{aligned} \mathcal{Q}_{\alpha\beta\gamma}^\nu &= \left. \frac{\partial^2}{\partial s \partial t} T_{\alpha\beta\gamma}^\nu[sR + tC] \right|_{s=t=0} \\ &= \text{Re} \sum_{\mu \neq \nu} \left[ U_{\alpha\beta\gamma}^{\nu\mu}[R, C] + U_{\alpha\beta\gamma}^{\nu\mu}[C, R] + U_{\beta\alpha\gamma}^{\nu\mu}[R, C] + U_{\beta\alpha\gamma}^{\nu\mu}[C, R] \right. \\ &\quad \left. - U_{\beta\gamma\alpha}^{\nu\mu}[R, C] - U_{\beta\gamma\alpha}^{\nu\mu}[C, R] \right. \\ &\quad \left. - \sum_{\eta \neq \mu, \nu} (V_{\alpha\beta\gamma}^{\nu\mu\eta}[R, C] + V_{\alpha\beta\gamma}^{\nu\mu\eta}[C, R]) \right]. \quad (\text{S42}) \end{aligned}$$

Since  $R$  is linear in the electric field and  $C$  in the magnetic field,  $\mathcal{Q}_{\alpha\beta\gamma}^\nu$  is the mixed  $EB$  contribution and yields the gauge-invariant second-order positional shift

$$a_\alpha^{(2, EB), \nu}(\mathbf{k}) = \mathcal{Q}_{\alpha\beta\gamma}^\nu(\mathbf{k}) E_\beta B_\gamma, \quad (\text{S43})$$

linear in both the electric field  $E_\beta$  and the magnetic field  $B_\gamma$ . To relate  $\mathcal{Q}$  to the cubic moment, the electric field entering Eq. (S43) in the perturbative normalization is the electric force  $\mathcal{E}_j = eE_j$ , and the mixed shift contributes

the  $\mathcal{E}^2 B$  energy  $+\frac{1}{2}\mathcal{E}_j\mathcal{E}_k B_i(\mathcal{Q}_{jki}^\nu + \mathcal{Q}_{kji}^\nu)$ , the factor 1/2 symmetrizing the two identical electric fields. Matching to the Zeeman form  $-B_i\delta m_{\nu,i}^{(2)}$  with  $\delta m_{\nu,i}^{(2)} = e^2 H_{ijk}^\nu E_j E_k$  gives

$$H_{ijk}^\nu = -\frac{1}{2}(\mathcal{Q}_{jki}^\nu + \mathcal{Q}_{kji}^\nu). \quad (\text{S44})$$

This 1/2 is the field-symmetrization factor for two identical electric fields, distinct from the 1/4 in Eq. (S30), which arose from antisymmetrization and the curl identity. The charge and symmetrization factors are therefore fixed by the chain

$$\begin{aligned} a_\alpha^{(2,EB),\nu} &= \mathcal{Q}_{\alpha\beta\gamma}^\nu E_\beta B_\gamma, & H_{ijk}^\nu &= -\frac{1}{2}(\mathcal{Q}_{jki}^\nu + \mathcal{Q}_{kji}^\nu), \\ \delta m_{\nu,i}^{(2)} &= e^2 H_{ijk}^\nu E_j E_k, & \beta_{ijkl}^{(H)} &= -e^3 \tau \sum_\nu \int_{\text{BZ}} \frac{d^d k}{(2\pi)^d} H_{ijk}^\nu v_l^\nu f_0'(\varepsilon_\nu), \end{aligned} \quad (\text{S45})$$

where  $v_l^\nu = \hbar^{-1}\partial_l\varepsilon_\nu$  is the band velocity,  $f_0$  is the equilibrium Fermi function, and  $\tau$  is the relaxation time.

#### S4. ORDERED OCCUPATION DYNAMICS AND FULL LOW-FREQUENCY FORMULAS

We next collect the ordered low-frequency Boltzmann contributions. This construction is logically distinct from the diagrammatic Kubo route of Secs. S1–S5; it builds the magnetization from a wave-packet kinetic chain with a *field-dressed* local orbital moment  $\tilde{m}_{\nu,i}$  and recovers the same three dc contributions. The equivalence holds only when the second-order positional-shift correction  $\delta m^{(2)}$  entering the mixed-quadrupole contribution and the metric-induced energy shift  $\delta\varepsilon^{(2)}$  entering the metric contribution are retained explicitly. Let  $f_0(\varepsilon_\nu)$  be the equilibrium Fermi function,  $f_0' \equiv \partial_\varepsilon f_0$ , and  $v_l^\nu(\mathbf{k}) \equiv (1/\hbar)\partial_l\varepsilon_\nu(\mathbf{k})$  the band velocity, and let  $\delta\tilde{f}_{\nu,r\dots 3}^{(n)}$  denote the  $n$ th-order occupation correction of band  $\nu$  for a fixed field ordering. The ordered Boltzmann chain is generated recursively by the standard semiclassical logic of nonlinear Hall and magneto-optical transport [5, 66, 67, 82]

$$[-i(\omega_r + \dots + \omega_3) + \tau^{-1}] \delta\tilde{f}_{\nu,r\dots 3}^{(n)} = -\frac{e}{\hbar} E_r \partial_r \delta\tilde{f}_{\nu,(r+1)\dots 3}^{(n-1)}, \quad (\text{S46})$$

with  $\delta\tilde{f}_\nu^{(0)} = f_0(\varepsilon_\nu)$  and  $\partial_r \equiv \partial/\partial k_r$ , where the label  $r$  marks the next field insertion in the ordered chain. For the ordered triple  $(j, \omega_1), (k, \omega_2), (l, \omega_3)$  we obtain

$$\delta\tilde{f}_{\nu,l}^{(1)} = -\frac{e\tau}{1 - i\omega_3\tau} E_l v_l^\nu f_0'(\varepsilon_\nu), \quad (\text{S47})$$

$$\delta\tilde{f}_{\nu,kl}^{(2)} = \frac{e^2\tau^2}{\hbar} E_k E_l \frac{\partial_k [v_l^\nu f_0'(\varepsilon_\nu)]}{[1 - i(\omega_2 + \omega_3)\tau][1 - i\omega_3\tau]}, \quad (\text{S48})$$

$$\delta\tilde{f}_{\nu,jkl}^{(3)} = -\frac{e^3\tau^3}{\hbar^2} E_j E_k E_l \frac{\partial_j \partial_k [v_l^\nu f_0'(\varepsilon_\nu)]}{(1 - i\Omega\tau)[1 - i(\omega_2 + \omega_3)\tau][1 - i\omega_3\tau]}. \quad (\text{S49})$$

The electric-field part of the second-order wave-packet energy is controlled by the gap-weighted (band-normalized) metric

$$\mathcal{G}_{jk}^\nu(\mathbf{k}) = 2 \text{Re} \sum_{\mu \neq \nu} \frac{A_{\nu\mu}^j(\mathbf{k}) A_{\mu\nu}^k(\mathbf{k})}{\Delta_{\nu\mu}(\mathbf{k})} = 2 \text{Re} \sum_{\mu \neq \nu} \frac{\langle \nu | \partial_j H | \mu \rangle \langle \mu | \partial_k H | \nu \rangle}{\Delta_{\nu\mu}^3(\mathbf{k})}, \quad (\text{S50})$$

a symmetric tensor that follows from nondegenerate second-order perturbation theory and controls the static electric polarizability of band  $\nu$  [79, 81]. Thus

$$\delta\varepsilon_\nu^{(2)}(\mathbf{k}) = \frac{e^2}{2} \mathcal{G}_{jk}^\nu(\mathbf{k}) E_j E_k, \quad (\text{S51})$$

which acts as an additional source term in the ordered Boltzmann equation and gives

$$\delta\tilde{f}_{\nu,jkl}^{(G)} = -\frac{e^3\tau}{2\hbar} E_j E_k E_l \frac{\partial_l [\mathcal{G}_{jk}^\nu(\mathbf{k}) f_0'(\varepsilon_\nu)]}{1 - i\Omega\tau}, \quad (\text{S52})$$

the label ( $G$ ) marking the occupation correction sourced by the metric energy shift. We combine this with the moment expansion

$$\tilde{m}_{\nu,i} = m_i^\nu + \delta m_{\nu,i}^{(1)} + \delta m_{\nu,i}^{(2)} + \dots, \quad M_i = \frac{1}{V} \sum_{\nu,\mathbf{k}} \tilde{m}_{\nu,i} f_\nu, \quad (\text{S53})$$

where  $\tilde{m}_{\nu,i}$  is the field-dressed local orbital moment,  $f_\nu$  the occupation of band  $\nu$ , and  $M_i$  the magnetization density. The equilibrium Berry-curvature contribution to  $M_i$  does not generate an independent cubic dc term; after integration by parts it is absorbed into the field-dressed moment and band energy of the mixed-quadrupole and metric contributions.

For the ordered triple  $(j, \omega_1), (k, \omega_2), (l, \omega_3)$ , define the ordered moment kernels

$$\delta m_{\nu,i,j}^{(1)}(\mathbf{k}, \omega_1) = \mathcal{M}_{ij}^\nu(\mathbf{k}, \omega_1) E_j, \quad \delta m_{\nu,i,jk}^{(2)}(\mathbf{k}, \omega_1, \omega_2) = \mathcal{N}_{ijk}^\nu(\mathbf{k}, \omega_1, \omega_2) E_j E_k.$$

At the adiabatic order retained, the first-order electric positional shift is  $a_a^{(1,E),\nu}(\mathbf{k}) = e \mathcal{G}_{aj}^\nu(\mathbf{k}) E_j$ , consistent with the charge counting in Eq. (S51), and the induced first-order moment is

$$\delta m_{\nu,i}^{(1)} = -\frac{e}{2} \epsilon_{iab} a_a^{(1,E),\nu}(\mathbf{k}) v_b^\nu(\mathbf{k}) = \mathcal{M}_{ij}^\nu(\mathbf{k}, 0) E_j, \quad \mathcal{M}_{ij}^\nu(\mathbf{k}, 0) = -\frac{e^2}{2} \epsilon_{iab} \mathcal{G}_{aj}^\nu(\mathbf{k}) v_b^\nu(\mathbf{k}).$$

This  $\mathcal{M} \times \delta f^{(2)}$  term is retained in Eq. (S54) for a generic noncentrosymmetric magnetic crystal. The mixed quadrupolar shift of Eq. (S44) gives

$$\mathcal{N}_{ijk}^\nu(\mathbf{k}, 0, 0) = e^2 H_{ijk}^\nu(\mathbf{k}).$$

The tensor below uses the leading static limits  $\mathcal{M}_{ij}^\nu(\mathbf{k}, \omega_1) = \mathcal{M}_{ij}^\nu(\mathbf{k}, 0) + \mathcal{O}(\omega_1)$  and  $\mathcal{N}_{ijk}^\nu(\mathbf{k}, \omega_1, \omega_2) = e^2 H_{ijk}^\nu(\mathbf{k}) + \mathcal{O}(\omega_1, \omega_2)$ . Keeping only terms third order in the fields,

$$\delta \tilde{M}_{i,jkl}^{(3)} = \frac{1}{V} \sum_{\nu,\mathbf{k}} \left[ \delta m_{\nu,i,jk}^{(2)} \delta \tilde{f}_{\nu,l}^{(1)} + \delta m_{\nu,i,j}^{(1)} \delta \tilde{f}_{\nu,kl}^{(2)} + m_i^\nu \delta \tilde{f}_{\nu,jkl}^{(G)} + m_i^\nu \delta \tilde{f}_{\nu,jkl}^{(3)} \right],$$

and substituting Eqs. (S47), (S48), (S49), and (S52) and removing the common factor  $E_j E_k E_l$  gives

$$\begin{aligned} \tilde{\beta}_{ijkl}^{\text{low}}(\Omega, \omega_1, \omega_2, \omega_3) &= -\frac{e\tau}{V} \sum_{\nu,\mathbf{k}} \frac{\mathcal{N}_{ijk}^\nu(\mathbf{k}, \omega_1, \omega_2) v_l^\nu(\mathbf{k}) f_0'(\varepsilon_\nu)}{1 - i\omega_3\tau} \\ &+ \frac{e^2\tau^2}{\hbar V} \sum_{\nu,\mathbf{k}} \frac{\mathcal{M}_{ij}^\nu(\mathbf{k}, \omega_1) \partial_k [v_l^\nu(\mathbf{k}) f_0'(\varepsilon_\nu)]}{[1 - i(\omega_2 + \omega_3)\tau](1 - i\omega_3\tau)} \\ &- \frac{e^3\tau}{2\hbar V} \sum_{\nu,\mathbf{k}} \frac{m_i^\nu(\mathbf{k}) \partial_l [\mathcal{G}_{jk}^\nu(\mathbf{k}) f_0'(\varepsilon_\nu)]}{1 - i\Omega\tau} \\ &- \frac{e^3\tau^3}{\hbar^2 V} \sum_{\nu,\mathbf{k}} \frac{m_i^\nu(\mathbf{k}) \partial_j \partial_k [v_l^\nu(\mathbf{k}) f_0'(\varepsilon_\nu)]}{(1 - i\Omega\tau)[1 - i(\omega_2 + \omega_3)\tau](1 - i\omega_3\tau)}. \end{aligned} \quad (\text{S54})$$

This decomposition is compatible with recent third-order transport formulations that isolate distinct quantum-geometric contributions [18, 19, 83]. In a nonmagnetic time-reversal-symmetric crystal the second ( $\mathcal{M} \delta f^{(2)}$ ) term is odd in  $\mathbf{k}$  and integrates to zero, leaving the surviving ordered tensor

$$\tilde{\beta}_{ijkl}^{\text{low,TR}}(\Omega, \omega_1, \omega_2, \omega_3) = \tilde{\beta}_{ijkl}^{\text{low}}(\Omega, \omega_1, \omega_2, \omega_3) \Big|_{\mathcal{M}_{ij}^\nu \rightarrow 0}, \quad (\text{S55})$$

i.e. the first, third, and fourth lines of Eq. (S54). The denominators belong to the ordered insertion  $(j, \omega_1), (k, \omega_2), (l, \omega_3)$ . The measured nondegenerate response follows from the paired-label symmetrization in Eq. (S15), which in the dc or degenerate THG limit reduces to ordinary symmetrization over the last three Cartesian indices.

In the strict dc limit,

$$\begin{aligned}\tilde{\beta}_{ijkl}^{\text{dc,TR}} &= \frac{e^3\tau}{2V} \sum_{\nu,\mathbf{k}} [\mathcal{Q}_{jki}^\nu(\mathbf{k}) + \mathcal{Q}_{kji}^\nu(\mathbf{k})] v_l^\nu(\mathbf{k}) f_0'(\varepsilon_\nu) \\ &\quad - \frac{e^3\tau}{2\hbar V} \sum_{\nu,\mathbf{k}} m_i^\nu(\mathbf{k}) \left[ (\Gamma_{j,lk}^{(\mathcal{G}),\nu} + \Gamma_{k,lj}^{(\mathcal{G}),\nu}) f_0'(\varepsilon_\nu) + \hbar \mathcal{G}_{jk}^\nu(\mathbf{k}) v_l^\nu(\mathbf{k}) f_0''(\varepsilon_\nu) \right] \\ &\quad - \frac{e^3\tau^3}{\hbar^2 V} \sum_{\nu,\mathbf{k}} m_i^\nu(\mathbf{k}) \partial_j \partial_k [v_l^\nu(\mathbf{k}) f_0'(\varepsilon_\nu)],\end{aligned}\tag{S56}$$

where

$$\Gamma_{c,ab}^{(\mathcal{G}),\nu} = \frac{1}{2} (\partial_a \mathcal{G}_{bc}^\nu + \partial_b \mathcal{G}_{ac}^\nu - \partial_c \mathcal{G}_{ab}^\nu)\tag{S57}$$

is the lowered-index Christoffel combination of the symmetric band-normalized metric, satisfying  $\Gamma_{j,lk}^{(\mathcal{G}),\nu} + \Gamma_{k,lj}^{(\mathcal{G}),\nu} = \partial_l \mathcal{G}_{jk}^\nu$ , the identity used in Eq. (S56). For a two-band model,  $g_{jk}^\nu$  is the usual quantum metric and  $\Delta_{\nu\bar{\nu}} \equiv \varepsilon_\nu - \varepsilon_{\bar{\nu}}$  the signed separation to the partner band  $\bar{\nu}$ ,

$$\mathcal{G}_{jk}^\nu = \frac{2}{\Delta_{\nu\bar{\nu}}} g_{jk}^\nu,\tag{S58}$$

so that

$$\partial_l \mathcal{G}_{jk}^\nu = \frac{2}{\Delta_{\nu\bar{\nu}}} (\Gamma_{j,lk}^\nu + \Gamma_{k,lj}^\nu) - \frac{2\partial_l \Delta_{\nu\bar{\nu}}}{\Delta_{\nu\bar{\nu}}^2} g_{jk}^\nu.\tag{S59}$$

with  $\Gamma_{c,ab}^\nu$  the first-kind Christoffel symbols of  $g^\nu$ , defined as in Eq. (S57) with  $\mathcal{G}^\nu \rightarrow g^\nu$ . The metric-drift contribution can therefore be reorganized partly in Christoffel form, with an additional gap-derivative term remaining. For related geometric viewpoints on nonlinear response and Christoffel-type nonlinear magnetization, see Refs. [23, 24, 52].

### A. Integral and multipole form of Eq. (S56)

To expose the geometric structure of Eq. (S56), write

$$\tilde{\beta}_{ijkl}^{\text{dc,TR}} = \beta_{ijkl}^{(H)} + \beta_{ijkl}^{(G)} + \beta_{ijkl}^{(\text{tr})},$$

where  $\beta^{(H)}$  is the mixed-quadrupole contribution,  $\beta^{(G)}$  the metric or Christoffel contribution, and  $\beta^{(\text{tr})}$  the purely transport contribution. The  $f_0''$  term in Eq. (S56) comes from the chain rule  $\partial_l [\mathcal{G}_{jk}^\nu f_0'(\varepsilon_\nu)] = (\partial_l \mathcal{G}_{jk}^\nu) f_0' + \hbar \mathcal{G}_{jk}^\nu v_l^\nu f_0''$ . Using  $V^{-1} \sum_{\mathbf{k}} \rightarrow \int_{\text{BZ}} d^d k / (2\pi)^d$  and integrating by parts, the explicit Brillouin-zone integrals are

$$\begin{aligned}\beta_{ijkl}^{(H)} &= -e^3\tau \sum_{\nu} \int_{\text{BZ}} \frac{d^d k}{(2\pi)^d} H_{ijk}^\nu(\mathbf{k}) v_l^\nu(\mathbf{k}) f_0'(\varepsilon_\nu) \\ &= \frac{e^3\tau}{\hbar} \sum_{\nu} \int_{\text{BZ}} \frac{d^d k}{(2\pi)^d} f_0(\varepsilon_\nu) \partial_l H_{ijk}^\nu(\mathbf{k}) \\ &= -\frac{e^3\tau}{2\hbar} \sum_{\nu} \int_{\text{BZ}} \frac{d^d k}{(2\pi)^d} f_0(\varepsilon_\nu) \partial_l [\mathcal{Q}_{jki}^\nu(\mathbf{k}) + \mathcal{Q}_{kji}^\nu(\mathbf{k})],\end{aligned}\tag{S60}$$

$$\begin{aligned}\beta_{ijkl}^{(G)} &= -\frac{e^3\tau}{2\hbar} \sum_{\nu} \int_{\text{BZ}} \frac{d^d k}{(2\pi)^d} m_i^\nu(\mathbf{k}) \partial_l [\mathcal{G}_{jk}^\nu(\mathbf{k}) f_0'(\varepsilon_\nu)] \\ &= \frac{e^3\tau}{2\hbar} \sum_{\nu} \int_{\text{BZ}} \frac{d^d k}{(2\pi)^d} (\partial_l m_i^\nu(\mathbf{k})) \mathcal{G}_{jk}^\nu(\mathbf{k}) f_0'(\varepsilon_\nu),\end{aligned}\tag{S61}$$

$$\begin{aligned}\beta_{ijkl}^{(\text{tr})} &= -\frac{e^3\tau^3}{\hbar^2} \sum_{\nu} \int_{\text{BZ}} \frac{d^d k}{(2\pi)^d} m_i^\nu(\mathbf{k}) \partial_j \partial_k [v_l^\nu(\mathbf{k}) f_0'(\varepsilon_\nu)] \\ &= \frac{e^3\tau^3}{\hbar^3} \sum_{\nu} \int_{\text{BZ}} \frac{d^d k}{(2\pi)^d} f_0(\varepsilon_\nu) \partial_j \partial_k \partial_l m_i^\nu(\mathbf{k}).\end{aligned}\tag{S62}$$

Equations (S60)–(S62) agree with the kernel-method forms Eqs. (S85), (S84), and (S83) derived in Sec. S5, so the Boltzmann and diagrammatic routes give the same three contributions. In the zero-temperature limit  $f'_0 = -\delta(\varepsilon_\nu - \mu)$ , and Eq. (S60) reduces to the Fermi-surface form

$$\beta_{ijkl}^{(H)} = \frac{e^3 \tau}{\hbar} \sum_\nu \int_{\text{FS}_\nu} \frac{dS}{(2\pi)^d} H_{ijk}^\nu(\mathbf{k}) \hat{n}_l^\nu(\mathbf{k}), \quad (\text{S63})$$

with  $\hat{n}_l^\nu(\mathbf{k}) = \partial_l \varepsilon_\nu(\mathbf{k}) / |\nabla_{\mathbf{k}} \varepsilon_\nu(\mathbf{k})|$ . Likewise,

$$\beta_{ijkl}^{(G)} = -\frac{e^3 \tau}{2\hbar} \sum_\nu \int_{\text{FS}_\nu} \frac{dS}{(2\pi)^d} \frac{(\partial_l m_i^\nu) \mathcal{G}_{jk}^\nu}{|\nabla_{\mathbf{k}} \varepsilon_\nu|}, \quad (\text{S64})$$

so the metric/Christoffel contribution is explicitly a Fermi-surface object weighted by the gradient of the local orbital moment.

For the two-band reduction and for comparison with conventional nonlinear-Hall language, introduce the axial Berry curvature and the band orbital moment,

$$\Omega_i^\nu(\mathbf{k}) = \frac{1}{2} \epsilon_{iab} F_{ab}^\nu(\mathbf{k}) = -\epsilon_{iab} \text{Im} \sum_{\mu \neq \nu} \frac{\langle \nu | \partial_a H | \mu \rangle \langle \mu | \partial_b H | \nu \rangle}{\Delta_{\nu\mu}^2(\mathbf{k})}, \quad (\text{S65})$$

$$m_i^\nu(\mathbf{k}) = -\frac{e}{2\hbar} \epsilon_{iab} \text{Im} \sum_{\mu \neq \nu} \frac{\langle \nu | \partial_a H | \mu \rangle \langle \mu | \partial_b H | \nu \rangle}{\Delta_{\nu\mu}(\mathbf{k})}, \quad (\text{S66})$$

with  $F_{ab}^\nu$  the Berry curvature. Only two occupied-state multipoles are needed for the dc formulas,

$$D_{l|ijk}^{(H)} = \sum_\nu \int_{\text{BZ}} \frac{d^d k}{(2\pi)^d} f_0(\varepsilon_\nu) \partial_l H_{ijk}^\nu, \quad O_{jkli}^{(m)} = \sum_\nu \int_{\text{BZ}} \frac{d^d k}{(2\pi)^d} f_0(\varepsilon_\nu) \partial_j \partial_k \partial_l m_i^\nu, \quad (\text{S67})$$

so that Eqs. (S60) and (S62) become

$$\beta_{ijkl}^{(H)} = \frac{e^3 \tau}{\hbar} D_{l|ijk}^{(H)}, \quad \beta_{ijkl}^{(\text{tr})} = \frac{e^3 \tau^3}{\hbar^3} O_{jkli}^{(m)}. \quad (\text{S68})$$

The tensor  $H_{ijk}^\nu$ , or equivalently  $\mathcal{Q}_{\alpha\beta\gamma}^\nu$ , is a mixed electric and magnetic quadrupolar shift of the wave packet.

For the two-band reduction it is convenient to write the usual quantum metric explicitly as

$$g_{jk}^\nu(\mathbf{k}) = \text{Re} \sum_{\mu \neq \nu} A_{\nu\mu}^j(\mathbf{k}) A_{\mu\nu}^k(\mathbf{k}) = \text{Re} \sum_{\mu \neq \nu} \frac{\langle \nu | \partial_j H | \mu \rangle \langle \mu | \partial_k H | \nu \rangle}{\Delta_{\nu\mu}^2(\mathbf{k})}. \quad (\text{S69})$$

This is the band-projected Fubini-Study quantum metric of Provost and Vallée [84], standard in the band-geometric and quantum-information literature; see Refs. [47, 85] for reviews. With a single partner band  $\bar{\nu}$ , Eqs. (S65) and (S66) imply

$$m_i^\nu = \frac{e \Delta_{\nu\bar{\nu}}}{2\hbar} \Omega_i^\nu, \quad (\text{S70})$$

which together with Eq. (S58) closes the two-band reduction. The metric contribution then becomes

$$\beta_{ijkl}^{(G)} = \frac{e^4 \tau}{2\hbar^2} \sum_\nu \int_{\text{BZ}} \frac{d^d k}{(2\pi)^d} g_{jk}^\nu(\mathbf{k}) \left[ \partial_l \Omega_i^\nu(\mathbf{k}) + \Omega_i^\nu(\mathbf{k}) \partial_l \ln \Delta_{\nu\bar{\nu}}(\mathbf{k}) \right] f'_0(\varepsilon_\nu), \quad (\text{S71})$$

a quantum-metric dressing of a Berry-curvature dipole plus a correction controlled by the gradient of the interband gap, and the transport contribution becomes

$$\beta_{ijkl}^{(\text{tr})} = \frac{e^4 \tau^3}{2\hbar^4} \sum_\nu \int_{\text{BZ}} \frac{d^d k}{(2\pi)^d} f_0(\varepsilon_\nu) \partial_j \partial_k \partial_l [\Delta_{\nu\bar{\nu}}(\mathbf{k}) \Omega_i^\nu(\mathbf{k})]. \quad (\text{S72})$$

For a momentum-dependent gap, expanding the derivative in Eq. (S72) generates gap-gradient corrections to a pure Berry-curvature octupole, so the compact form is more transparent than the full derivative hierarchy. The mixed-quadrupole contribution does not admit a universal reduction to conventional Berry-curvature multipoles; its natural form is the dipole of the gauge-invariant mixed quadrupole  $H_{ijk}^\nu$ .

## S5. DIAGRAMMATIC ORIGIN OF THE THREE DC CONTRIBUTION FORMULAS

The semiclassical Boltzmann construction in Sec. S4 reaches the three dc contribution formulas  $\beta_{ijkl}^{(H)}$ ,  $\beta_{ijkl}^{(G)}$ , and  $\beta_{ijkl}^{(\text{tr})}$  through a wave-packet kinetic equation and a field-dressed orbital moment. This section gives the corresponding Ward-covariant diagrammatic origin in the Matsubara kernel of Eq. (S23). The goal is not to assign physical meaning to individual non-gauge-invariant diagrams before recombination. Rather, it shows how the full 26-term kernel reorganizes into the three covariant objects of Eq. (S32). We use (i) the band-resolved spectral form of  $G$ , (ii) the standard contour identity for fermionic Matsubara sums, (iii) the ordered retarded analytic continuation of Eq. (S28), and (iv) phenomenological scalar relaxation  $i\omega_r \rightarrow \omega_r + i/\tau$  at intraband resonances, applied only after the Ward-complete clean kernel has been organized.

*Step 1 Band-resolved spectral form of  $G$  and of every vertex.* Diagonalize the Bloch Hamiltonian,  $h(\mathbf{k})|u_\nu(\mathbf{k})\rangle = \varepsilon_\nu(\mathbf{k})|u_\nu(\mathbf{k})\rangle$ . With  $\xi_\nu(\mathbf{k}) \equiv \varepsilon_\nu(\mathbf{k}) - \mu$  the Green function is band-diagonal,

$$G_K^{\nu\mu}(i\nu_n) = \frac{\delta_{\nu\mu}}{i\nu_n - \xi_\nu(\mathbf{k})}. \quad (\text{S73})$$

Differentiating  $h|u_\nu\rangle = \varepsilon_\nu|u_\nu\rangle$  once in  $k_a$  and projecting (Hellmann and Feynman) gives

$$\langle \nu | \partial_a h | \mu \rangle = \begin{cases} \partial_a \varepsilon_\nu \equiv \hbar v_a^\nu, & \nu = \mu, \\ i \Delta_{\nu\mu} A_{\nu\mu}^a, & \nu \neq \mu, \end{cases} \quad (\text{S74})$$

with  $A_{\mu\nu}^a = \langle \mu | i \partial_a | \nu \rangle$  the interband Berry connection of Eq. (S34). The current vertices (S8) through (S11) therefore split, in band basis, into intraband (band-dispersion) and interband (Berry-connection-weighted) pieces. The contact vertices  $\Gamma^{(2)}, \Gamma^{(3)}, \Gamma^{(4)}$  are local in  $\mathbf{k}$ . They contain no propagator factors and enter the Matsubara sums as plain matrix elements.

*Step 2 Action of  $\partial/\partial q_b$  at  $\mathbf{q} = 0$ .* In the continuum shorthand, after the Ward-complete finite- $q$  vertices have been reduced to their  $q \rightarrow 0$  covariant form, the explicit output spatial momentum  $\mathbf{q}$  enters Eq. (S23) through the response-leg propagator  $G_{K+Q}$ . Differentiating the inverse Green function and using  $\partial_b G^{-1} = -\partial_b h$ ,

$$\left. \frac{\partial G_{K+Q}}{\partial q_b} \right|_{\mathbf{q}=0} = G_{K+\bar{Q}} (\partial_b h) G_{K+\bar{Q}} = \frac{\hbar}{e} G_{K+\bar{Q}} \Gamma_b^{(1)} G_{K+\bar{Q}}, \quad (\text{S75})$$

where  $\bar{Q} = Q_1 + Q_2 + Q_3$  has zero spatial part at  $\mathbf{q} = 0$ . Thus this propagator part of  $\partial_b$  duplicates the response-leg propagator and inserts an extra  $\Gamma_b^{(1)}$  vertex. In a Peierls lattice implementation, however, Eq. (S22) shows that  $\partial_b$  also differentiates the finite- $q$  vertex form factors. Those vertex-derivative pieces are included in the Ward-complete numerical kernel and cancel against contact terms in the longitudinal contribution. The analytic reduction below uses Eq. (S75) only after this Ward-complete  $q \rightarrow 0$  organization, and not as a statement that finite- $q$  vertex derivatives vanish term by term on the lattice.

*Step 3 Antisymmetric  $\epsilon_{cab}$  projection selects interband response-leg pairings.* The combination of vertices entering  $\epsilon_{cab} \Gamma_a^{(1)}$  and the  $\partial_b$ -induced  $\Gamma_b^{(1)}$  on the response leg is, in band basis,

$$\Lambda_c^{\nu\mu} \equiv \epsilon_{cab} \langle \nu | \partial_a h | \mu \rangle \langle \mu | \partial_b h | \nu \rangle. \quad (\text{S76})$$

Because  $\epsilon_{cab} v_a^\nu v_b^\nu = 0$ , the intraband-intraband contribution to  $\Lambda_c^{\nu\mu}$  vanishes identically. The antisymmetric projection therefore forces at least one of the two response-leg pairings to be interband ( $\mu \neq \nu$ ). This is the kernel-level statement that the bulk magnetization is fundamentally a band-geometric quantity, and a fully diagonal box does not contribute to it.

*Step 4 Matsubara sum and the entry of  $f_0$ .* Each diagram of Eqs. (S24) through (S27), after band labels are assigned to the propagators, produces an integrand of the form  $F(i\nu_n) = \prod_{r=1}^n 1/(i\nu_n + i\Omega_r - \xi_r)$ , with bosonic  $i\Omega_r$  and band energies  $\xi_r$ . The approach is the standard residue identity for fermionic Matsubara sums

$$\frac{1}{\beta_T} \sum_{\nu_n} F(i\nu_n) = \sum_{z_p} n_F(z_p) \text{Res}_{z=z_p} F(z), \quad n_F(z) = \frac{1}{e^{\beta_T z} + 1}, \quad (\text{S77})$$

where the sum on the right runs over the poles  $z_p$  of  $F(z)$ . For  $F(z) = \prod_r (z + i\Omega_r - \xi_r)^{-1}$  these poles are  $z_r = \xi_r - i\Omega_r$ , and the residue formula gives

$$\frac{1}{\beta_T} \sum_{\nu_n} F(i\nu_n) = \sum_{r=1}^n n_F(\xi_r - i\Omega_r) \prod_{s \neq r} \frac{1}{(\xi_r - \xi_s) - i(\Omega_r - \Omega_s)}. \quad (\text{S78})$$

Since each  $i\Omega_r$  is a bosonic Matsubara frequency,  $n_F(\xi_r - i\Omega_r) = n_F(\xi_r) \equiv f_0(\varepsilon_r)$ . When several band energies coalesce, the residue sum is a divided difference of  $f_0$ . In particular,

$$\lim_{\xi_1, \dots, \xi_n \rightarrow \xi} \sum_{r=1}^n f_0(\xi_r) \prod_{s \neq r} \frac{1}{\xi_r - \xi_s} = \frac{1}{(n-1)!} \frac{d^{n-1} f_0}{d\xi^{n-1}}, \quad (\text{S79})$$

with the finite external frequencies and the relaxation broadening regulating the intermediate Drude denominators.

*Step 5 Pole-topology classification.* The Drude denominator  $\prod_{s \neq r} 1/[(\xi_r - \xi_s) - (\omega_r - \omega_s)]$  depends on the band assignment. For the box class  $\tilde{\mathcal{B}}$ , group configurations by the topology of repeated band labels

- (A) all four bands equal,  $(\nu, \nu, \nu, \nu)$ . After  $\partial_b$ , the augmented loop adds a fifth, possibly interband, propagator.
- (B) two equal pairs,  $(\nu, \nu, \mu, \mu)$  with  $\mu \neq \nu$ .
- (C) three equal plus one different,  $(\nu, \nu, \nu, \mu)$ .
- (D) all four distinct.

Topology (D) carries no intraband Drude factors. It is finite as  $\omega_r \rightarrow 0$  and is largely cancelled by the Ward-completing contact terms  $\tilde{\mathcal{C}}, \tilde{\mathcal{D}}, \tilde{\mathcal{Q}}$ . Topology (C) has one mismatched band index. After expanding the four-pole Matsubara residue (S78) in the dc limit, the divided-difference identity (S79) collapses the three repeated-band poles to derivatives of  $f_0$  on band  $\nu$  while the mismatched index supplies a single interband factor  $\propto 1/\Delta_{\nu\mu}$ . Integration by parts in the Brillouin zone then redistributes these contributions into pieces structurally identical to (A) (when the derivative lands on band- $\nu$  quantities) or (B) (when it lands on the interband residue). The leading dc structure is therefore captured by topologies (A) and (B), plus a separate contribution from the contact families with no analog in  $\tilde{\mathcal{B}}$ .

*Step 6 dc limit and  $\tau$ -broadening.* For repeated band labels ( $\xi_r = \xi_s$ ) the Drude denominator becomes  $1/[-(\omega_r - \omega_s)]$  and is singular as  $\omega_r \rightarrow \omega_s$ . Phenomenological relaxation regularizes the singularity

$$\frac{1}{-(\omega_r - \omega_s) + i0^+} \rightarrow \frac{1}{-(\omega_r - \omega_s) + i/\tau}. \quad (\text{S80})$$

Within this scalar relaxation-time approximation, in the dc limit  $\omega_r \rightarrow 0$ , each such factor  $\rightarrow -i\tau$ . Counting the intraband factors in each topology gives  $(-i\tau)^3 = i\tau^3$  for (A),  $-i\tau$  for (B), and zero  $\tau$ -dependence for (D). The vector-potential kernel also contains one Ward zero for each incoming electric leg. Hence, before division by  $\omega_1\omega_2\omega_3$  in Eq. (S32), the projected contribution has the schematic form

$$\epsilon_{cab} [\partial_{q_b} \tilde{K}_{a,jkl}^{R,X} - \partial_{q_a} \tilde{K}_{b,jkl}^{R,X}]_{q=0} = 4\omega_1\omega_2\omega_3 \beta_{c,jkl}^{(X)} + \mathcal{O}(\omega^4), \quad X = H, G, \text{tr}. \quad (\text{S81})$$

This is the explicit small-frequency zero that cancels the electric-field conversion denominator.

*Step 7 Topology (A)  $\Rightarrow$  the transport contribution  $\beta_{ijkl}^{(\text{tr})}$ .* Take the box  $\tilde{\mathcal{B}}$  with band assignment  $(\nu, \nu, \nu, \nu)$  on the four loop propagators. The  $\partial_b$ -induced extra propagator must be on the interband band  $\mu \neq \nu$  by the argument of Step 3 (otherwise the antisymmetrizer kills the term). The integrand factorizes as

$$[\text{intraband chain on band } \nu] \times [\text{single } \nu \rightarrow \mu \rightarrow \nu \text{ interband excursion}].$$

The three remaining  $\Gamma^{(1)}$  vertices on the loop interior give intraband factors  $(ev_j^\nu)(ev_k^\nu)(ev_l^\nu)$ . The  $\epsilon_{cab}$ -projected single-excursion piece collapses to the orbital moment via the band-resolved identity

$$\epsilon_{iab} \text{Im} \sum_{\mu \neq \nu} \frac{\langle \nu | \partial_a h | \mu \rangle \langle \mu | \partial_b h | \nu \rangle}{\Delta_{\nu\mu}} = -\frac{2\hbar}{e} m_i^\nu(\mathbf{k}), \quad (\text{S82})$$

which is the definition of the band orbital moment in Eq. (S66). The single  $1/\Delta_{\nu\mu}$  is the residue of the  $G^\mu$  propagator evaluated at the band- $\nu$  pole. The Matsubara sum at the four-coalesced pole, evaluated with the  $\tau$ -broadening of Eq. (S80), generates a series of intraband Drude factors and Taylor expansions of  $f_0$  at  $\varepsilon_\nu$ ,

$$f_0(\varepsilon_\nu), \quad \hbar v_l^\nu f_0'(\varepsilon_\nu), \quad \hbar^2 v_k^\nu v_l^\nu f_0''(\varepsilon_\nu), \quad \hbar^3 v_j^\nu v_k^\nu v_l^\nu f_0'''(\varepsilon_\nu),$$

which combine into the compact derivative  $\partial_j \partial_k (v_l^\nu f_0'(\varepsilon_\nu))$  by the chain rule  $\partial_l f_0(\varepsilon_\nu) = \hbar v_l^\nu f_0'(\varepsilon_\nu)$ . Substituting all factors into Eq. (S32) and using  $V^{-1} \sum_{\mathbf{k}} \rightarrow \int_{\text{BZ}} d^d k / (2\pi)^d$  gives, in the dc limit,

$$\beta_{ijkl}^{(\text{tr})} = -\frac{e^3 \tau^3}{\hbar^2} \sum_{\nu} \int_{\text{BZ}} \frac{d^d k}{(2\pi)^d} m_i^\nu(\mathbf{k}) \partial_j \partial_k [v_l^\nu(\mathbf{k}) f_0'(\varepsilon_\nu)]. \quad (\text{S83})$$

*Step 8 Topology (B)  $\Rightarrow$  the metric/Christoffel contribution  $\beta_{ijkl}^{(G)}$ .* Take the box with band assignment  $(\nu, \nu, \mu, \mu)$ , with two propagators on band  $\nu$  and two on band  $\mu$ . The four-pole Matsubara sum (S78) yields, in the leading dc-limit interband channel,

$$\frac{f_0(\varepsilon_\nu) - f_0(\varepsilon_\mu)}{\Delta_{\nu\mu}^2} + \frac{f'_0(\varepsilon_\nu) + f'_0(\varepsilon_\mu)}{\Delta_{\nu\mu}} + \dots$$

The two off-diagonal  $\partial h$  insertions on the  $\mu$  propagators contract via Eq. (S74) into  $-\Delta_{\nu\mu}^2 A_{\nu\mu}^j A_{\mu\nu}^k$ , which combines with the leading Matsubara factor to give  $A_{\nu\mu}^j A_{\mu\nu}^k / \Delta_{\nu\mu}$ , while the  $\Gamma^{(2)}$  contact pieces of  $\tilde{\mathcal{C}}$  cancel the residual longitudinal terms. Summing over  $\mu \neq \nu$  and taking the real part reproduces the band-normalized quantum metric of Eq. (S50),

$$2 \operatorname{Re} \sum_{\mu \neq \nu} \frac{A_{\nu\mu}^j A_{\mu\nu}^k}{\Delta_{\nu\mu}} f'_0(\varepsilon_\nu) = \mathcal{G}_{jk}^\nu(\mathbf{k}) f'_0(\varepsilon_\nu).$$

Diagrammatically, this configuration is the static second-order energy shift of band  $\nu$  in the electric field (S51), dressing the equilibrium occupation of band  $\nu$ . The remaining intraband Drude pole on band  $\nu$  on the response leg supplies one factor of  $-i\tau$  (the  $\tau^1$  scaling), the vertex  $\Gamma_l^{(1)} \rightarrow ev_l^\nu$  on that leg provides the band velocity, and the  $\epsilon_{cab}$ -antisymmetrized single virtual excursion produces  $m_i^\nu$  via Eq. (S82). Substituting into Eq. (S32) gives, in the dc limit,

$$\beta_{ijkl}^{(G)} = -\frac{e^3 \tau}{2\hbar} \sum_\nu \int_{\text{BZ}} \frac{d^d k}{(2\pi)^d} m_i^\nu(\mathbf{k}) \partial_l [\mathcal{G}_{jk}^\nu(\mathbf{k}) f'_0(\varepsilon_\nu)]. \quad (\text{S84})$$

Integration by parts in  $k_l$  (both  $m_i^\nu$  and  $\mathcal{G}_{jk}^\nu f'_0$  are periodic on the Brillouin zone) gives

$$\beta_{ijkl}^{(G)} = +\frac{e^3 \tau}{2\hbar} \sum_\nu \int_{\text{BZ}} \frac{d^d k}{(2\pi)^d} (\partial_l m_i^\nu) \mathcal{G}_{jk}^\nu f'_0(\varepsilon_\nu).$$

The Christoffel structure  $\Gamma_{j,lk}^{(\mathcal{G}),\nu} + \Gamma_{k,lj}^{(\mathcal{G}),\nu} = \partial_l \mathcal{G}_{jk}^\nu$  is implicit in the compact form. It surfaces only when one expands  $\partial_l [\mathcal{G}_{jk}^\nu f'_0] = (\partial_l \mathcal{G}_{jk}^\nu) f'_0 + \hbar \mathcal{G}_{jk}^\nu v_l^\nu f''_0$  inside Eq. (S56).

*Step 9 Contact and vertex-derivative families  $\Rightarrow$  the H contribution  $\beta_{ijkl}^{(H)}$ .* The primitive box class  $\tilde{\mathcal{B}}$  does not by itself contain the covariant mixed positional-shift tensor  $\mathcal{Q}_{\alpha\beta\gamma}^\nu$ . That tensor is built from  $U[R, C] + U[C, R]$  and, in multiband systems,  $V[R, C] + V[C, R]$ , which arise only after the Ward-complete set of contact vertices and finite- $q$  vertex derivatives has been combined. Thus the statement is not that an arbitrary box diagram can be discarded before enforcing gauge invariance. Rather, in the covariant organization used here the box topologies reduce to the transport and metric contributions, while the remaining mixed electric-magnetic positional-shift block is carried by the contact and finite- $q$  vertex contribution. A term-by-term contraction of all 26 diagrams into Eq. (S42) is not used as a separate assumption in the continuum estimate below. The mixed-quadrupole amplitude in the continuum model remains formal until the interband magnetic matrix element is fixed by a microscopic magnetic-coupling prescription or by a lattice completion.

Differentiating  $G^{-1}(A)$  twice with respect to the electric source amplitudes  $A_j, A_k$  and once with respect to a magnetic-source insertion is the diagrammatic counterpart of the wave-packet positional-shift functional (S40), restricted to the mixed  $EB$  contribution by the bookkeeping projection  $\partial_s \partial_t$  at  $s = t = 0$  in Eq. (S42). The  $\Gamma^{(2)}\Gamma^{(2)}$  double-contact subclass of  $\tilde{\mathcal{D}}$ , together with the associated finite- $q$  derivatives of the rank-two Peierls vertices, supplies the  $U[R, C] + U[C, R]$  building blocks. The  $\Gamma^{(3)}\Gamma^{(1)}$  cubic-contact subclass and the quartic contact  $\tilde{\mathcal{Q}}$  supply the remaining intermediate-band and symmetrization pieces required by Eq. (S42). After all band sums and matrix-element contractions, this Ward-complete contact contribution assembles into the gauge-invariant tensor  $H_{ijk}^\nu = -\frac{1}{2}[\mathcal{Q}_{jki}^\nu + \mathcal{Q}_{kji}^\nu]$  of Eq. (S44).

The remaining loop structure has a single propagator on band  $\nu$  on the response leg, carrying the response-frequency Drude factor  $1/(1 - i\omega_3\tau) \rightarrow 1$  in the dc limit (and the  $\tau^1$  scaling), the vertex  $\Gamma_l^{(1)} \rightarrow ev_l^\nu$ , and the Matsubara residue  $f'_0(\varepsilon_\nu)$  at the response-leg pole. Substituting into Eq. (S32) gives

$$\beta_{ijkl}^{(H)} = -e^3 \tau \sum_\nu \int_{\text{BZ}} \frac{d^d k}{(2\pi)^d} H_{ijk}^\nu(\mathbf{k}) v_l^\nu(\mathbf{k}) f'_0(\varepsilon_\nu). \quad (\text{S85})$$

TABLE S1. Ward-covariant origin of the three dc contributions in the direct kernel reduction. The entries describe the organization after the full 26-term kernel and the finite- $q$  Peierls vertex derivatives have been combined.

Contribution	Pole topology	Kernel ingredients	Covariant object
$\beta^{(\text{tr})}$	four intraband poles	box topology (A) plus Ward completion	orbital-moment octupole
$\beta^{(G)}$	two-pair interband topology	box topology (B) with rank-two contacts cancelling longitudinal pieces	metric drift
$\beta^{(H)}$	one intraband response pole	double-, cubic-, and quartic-contact families plus finite- $q$ vertex derivatives	$m_i^\nu \partial_l \mathcal{G}_{jk}^\nu$ or $\partial_l m_i^\nu \mathcal{G}_{jk}^\nu$ mixed electric-magnetic positional shift $H_{ijk}^\nu = -[\mathcal{Q}_{jki}^\nu + \mathcal{Q}_{kji}^\nu]/2$

## S6. SYMMETRY SELECTION RULES AND POINT-GROUP COMPONENT LISTS

Throughout this section  $\beta^{\text{phys}}$  denotes the permutation-symmetrized tensor defined in Eq. (S15). Because magnetization is axial and the electric field is polar, this physical tensor transforms under a point-group operation  $R \in O(3)$  as

$$\beta_{ijkl}^{\text{phys}} = \det(R) R_{ii'} R_{jj'} R_{kk'} R_{ll'} \beta_{i'j'k'l'}^{\text{phys}}. \quad (\text{S86})$$

Inversion  $R = -I$  therefore forces the uniform bulk tensor to vanish whenever the crystal is invariant under spatial inversion  $P$ ,

$$\beta_{ijkl}^{\text{phys}} = 0 \quad (\text{crystal is } P\text{-symmetric}). \quad (\text{S87})$$

The same tensor law is obeyed separately by the mixed-quadrupole contribution, the metric-drift contribution, and the transport contribution after Brillouin-zone integration. For tensor-based symmetry analysis of crystal response coefficients, see Ref. [86]. For recent nonlinear Hall-type symmetry discussions in the transport context, see Ref. [66].

Beyond point-group symmetry, antiunitary symmetries determine which low-frequency contributions survive, in line with the symmetry constraints emphasized in nonlinear Hall and related transport responses [19, 66]. The four ordered contributions in Eq. (S54) are (i)  $\delta m^{(2)} \delta f^{(1)}$ , the first line, with integrand  $\mathcal{N}_{ijk}^\nu v_l^\nu f_0'(\varepsilon_\nu)$ , (ii)  $\delta m^{(1)} \delta f^{(2)}$ , the second line, with integrand  $\mathcal{M}_{ij}^\nu \partial_k [v_l^\nu f_0'(\varepsilon_\nu)]$ , (iii)  $m \delta f^{(G)}$ , the third line, with integrand  $m_i^\nu \partial_l [\mathcal{G}_{jk}^\nu f_0'(\varepsilon_\nu)]$ , and (iv)  $m \delta f^{(3)}$ , the fourth line, with integrand  $m_i^\nu \partial_j \partial_k [v_l^\nu f_0'(\varepsilon_\nu)]$ . In the Abelian nonmagnetic class, or after pairing Kramers partners at  $\mathbf{k}$  and  $-\mathbf{k}$  in a spinful time-reversal-symmetric crystal, the  $\mathbf{k}$ -parities of  $m_i^\nu$ ,  $\mathcal{G}_{jk}^\nu$ , and  $v_l^\nu$  are

$$m_i^\nu(-\mathbf{k}) = -m_i^\nu(\mathbf{k}), \quad \mathcal{G}_{jk}^\nu(-\mathbf{k}) = \mathcal{G}_{jk}^\nu(\mathbf{k}), \quad v_l^\nu(-\mathbf{k}) = -v_l^\nu(\mathbf{k}), \quad (\text{S88})$$

supplemented by

$$\mathcal{N}_{ijk}^\nu(-\mathbf{k}) = -\mathcal{N}_{ijk}^\nu(\mathbf{k}). \quad (\text{S89})$$

This follows directly from the mixed electric-magnetic nature of the quadrupole. Under time reversal, after pairing  $|u_\nu(\mathbf{k})\rangle$  with its partner at  $-\mathbf{k}$ , the electric interband amplitude is even up to complex conjugation,  $R_{\bar{\mu}\bar{\nu}}^j(-\mathbf{k}) = [R_{\mu\nu}^j(\mathbf{k})]^*$ , whereas the magnetic amplitude is odd,  $C_{\bar{\mu}\bar{\nu}}^i(-\mathbf{k}) = -[C_{\mu\nu}^i(\mathbf{k})]^*$ . Each term in Eq. (S42) contains one  $R$  and one  $C$  and is finally real-part projected, hence  $\mathcal{Q}_{\alpha\beta\gamma}^\nu(-\mathbf{k}) = -\mathcal{Q}_{\alpha\beta\gamma}^\nu(\mathbf{k})$  and  $H_{ijk}^\nu(-\mathbf{k}) = -H_{ijk}^\nu(\mathbf{k})$ , which gives Eq. (S89) because  $\mathcal{N}_{ijk}^\nu(0,0) = e^2 H_{ijk}^\nu$ . Similarly,  $\mathcal{M}_{ij}^\nu(-\mathbf{k}) = -\mathcal{M}_{ij}^\nu(\mathbf{k})$  since  $\mathcal{M}_{ij}^\nu \propto \epsilon_{iab} \mathcal{G}_{aj}^\nu v_b^\nu$  contains a single power of  $v_b^\nu$ . Therefore the integrand of contribution (ii),  $\mathcal{M}_{ij}^\nu \partial_k [v_l^\nu f_0'(\varepsilon_\nu)]$ , is odd in  $\mathbf{k}$  (odd  $\times$  even), and the  $\delta m^{(1)} \delta f^{(2)}$  contribution drops out upon Brillouin-zone integration. The remaining three contributions, (i), (iii), and (iv), have integrands that are even in  $\mathbf{k}$  and survive. In a generic noncentrosymmetric magnetic class all four low-frequency contributions are allowed. In a  $PT$ -symmetric Abelian description one instead has  $m_i^\nu(\mathbf{k}) = 0$  and  $\mathcal{N}_{ijk}^\nu(\mathbf{k}) = 0$ , so only the  $\delta m^{(1)} \delta f^{(2)}$  contribution can survive. Table S2 summarizes these cases.

A natural question is whether some symmetry class can isolate the metric contribution alone. The three dc pieces  $\beta^{(H)}$ ,  $\beta^{(G)}$ , and  $\beta^{(\text{tr})}$  all transform identically (axial rank-four, odd under inversion), and the latter two share the factor  $m_i^\nu$ . Thus no antiunitary symmetry filters out only the non-metric pieces, and a purely metric response is not a distinct symmetry class. It can arise only through accidental microscopic cancellations on the active Fermi sheets.

For the model used here, the  $C_{3v}$  component list is the relevant one.

$C_{3v}$ .

$$\begin{aligned} \beta_{yxxx}^{\text{phys}} &= 3C_1, & \beta_{xyyy}^{\text{phys}} &= -3C_1, & \beta_{yxyy}^{\text{phys}} &= C_1, & \beta_{xxxy}^{\text{phys}} &= -C_1, \\ \beta_{yxxz}^{\text{phys}} &= C_2, & \beta_{xyzz}^{\text{phys}} &= -C_2, & \beta_{xxyz}^{\text{phys}} &= -C_3, & \beta_{yxxz}^{\text{phys}} &= -C_3, \\ \beta_{yyyz}^{\text{phys}} &= C_3, & \beta_{zyyy}^{\text{phys}} &= C_4, & \beta_{zxyy}^{\text{phys}} &= -C_4, & & \end{aligned} \quad (\text{S90})$$

TABLE S2. Low-frequency contribution selection by symmetry class.

Symmetry class	Surviving ordered low-frequency contributions
Centrosymmetric ( $P$ present)	none
Noncentrosymmetric, $T$ symmetric	$\delta m^{(2)} \delta f^{(1)}$ , $m \delta f^{(G)}$ , $m \delta f^{(3)}$
Noncentrosymmetric, $PT$ symmetric	$\delta m^{(1)} \delta f^{(2)}$ only
Generic noncentrosymmetric magnetic	all four
Pure metric/Christoffel limit	not a symmetry class by itself, additional microscopic constraints are required

again with permutations of the last three indices understood.

The component list above uses a convention in which one vertical mirror line is the  $x$  axis, so the mirror operation sends  $y \rightarrow -y$  while the axial component  $M_z$  changes sign. Restricting to in-plane fields in this convention leaves a single independent coefficient,

$$\beta_{zxxy}^{\text{phys}} = \beta_{zxyx}^{\text{phys}} = \beta_{zyxx}^{\text{phys}} \equiv \chi, \quad \beta_{zyyy}^{\text{phys}} = -\chi, \quad (\text{S91})$$

so that

$$M_z = \chi (3E_x^2 E_y - E_y^3) = +\chi E^3 \sin 3\phi, \quad \mathbf{E}_\omega = E(\cos \phi, \sin \phi, 0). \quad (\text{S92})$$

The orthogonal  $\cos 3\phi$  harmonic arises in the rotated convention used by the model Hamiltonian of Sec. S7. The two forms are related by a  $30^\circ$  rotation of the crystal axes relative to the laboratory field frame.

## S7. MINIMAL MODEL HAMILTONIAN FOR CUBIC-LEADING NONLINEAR MAGNETIZATION

The minimal model used below is a time-reversal-symmetric two-dimensional  $C_{3v}$  Hamiltonian for the out-of-plane magnetization generated by an in-plane electric field. Here  $M_z$  transforms as  $A_2$  and the in-plane electric field as the two-dimensional irrep  $E$ . The symmetric powers of  $E$  contain  $A_2$  first at cubic order, so the linear and quadratic contributions vanish and the cubic term is the leading response. A minimal Hamiltonian is

$$H_{C_{3v}}(\mathbf{k}) = \left( \frac{k_x^2 + k_y^2}{2m^*} - \mu \right) \sigma_0 + v(k_x \sigma_y - k_y \sigma_x) + \lambda(k_x^3 - 3k_x k_y^2) \sigma_z, \quad (\text{S93})$$

where  $m^*$  is the band mass,  $v$  the linear (Rashba) velocity, and  $\lambda$  the cubic warping amplitude. This Hamiltonian breaks inversion, preserves time-reversal symmetry, and produces a finite Fermi contour for  $\mu \neq 0$ . The cubic warping factor is

$$w(\mathbf{k}) = k_x^3 - 3k_x k_y^2 = k^3 \cos 3\phi.$$

The mirror lines of this Hamiltonian are rotated by  $30^\circ$  relative to the convention used in Eq. (S92). The warping factor  $\cos 3\phi$  is odd under reflection about the  $y$  axis, compensating the odd transformation of the axial spin component  $\sigma_z$ . Thus this model realizes the rotated  $C_{3v}$  harmonic

$$M_z = \bar{\chi} (E_x^3 - 3E_x E_y^2) = \bar{\chi} E_0^3 \cos 3\phi, \quad \mathbf{E} = E_0(\cos \phi, \sin \phi, 0). \quad (\text{S94})$$

The coefficient  $\chi$  defined in Eq. (S91) vanishes for Eq. (S93) as written. The nonzero cubic response is carried by the rotated coefficient  $\bar{\chi} = \bar{\chi}_H + \bar{\chi}_G + \bar{\chi}_{\text{tr}}$ , resolved into contributions below.

### A. Local geometry and cubic contributions for the model Hamiltonian (S93)

For the two-dimensional model Hamiltonian in Eq. (S93), it is convenient to rewrite

$$H_{C_{3v}}(\mathbf{k}) = \xi_{\mathbf{k}} \sigma_0 + \mathbf{d}(\mathbf{k}) \cdot \boldsymbol{\sigma}, \quad \xi_{\mathbf{k}} = \frac{k_x^2 + k_y^2}{2m^*} - \mu, \quad (\text{S95})$$

with

$$\mathbf{d}(\mathbf{k}) = (-vk_y, vk_x, \lambda w(\mathbf{k})), \quad w(\mathbf{k}) = k_x^3 - 3k_x k_y^2. \quad (\text{S96})$$

We write the band mass with an asterisk throughout to keep it distinct from the orbital magnetic moment  $m'_i$ . The band energies are

$$\varepsilon_s(\mathbf{k}) = \xi_{\mathbf{k}} + s\varepsilon(\mathbf{k}), \quad s = \pm, \quad \varepsilon(\mathbf{k}) = |\mathbf{d}(\mathbf{k})| = \sqrt{v^2(k_x^2 + k_y^2) + \lambda^2 w(\mathbf{k})^2}, \quad (\text{S97})$$

and the signed two-band gap is

$$\Delta_s(\mathbf{k}) = \varepsilon_s(\mathbf{k}) - \varepsilon_{-s}(\mathbf{k}) = 2s\varepsilon(\mathbf{k}). \quad (\text{S98})$$

For brevity we denote the partial derivatives of the cubic warping factor by  $w_i \equiv \partial_i w$ ,  $w_{ij} \equiv \partial_i \partial_j w$ , and  $w_{ijk} \equiv \partial_i \partial_j \partial_k w$ , all of which follow by direct differentiation of  $w(\mathbf{k}) = k_x^3 - 3k_x k_y^2$ . We further define

$$B_i(\mathbf{k}) \equiv v^2 k_i + \lambda^2 w(\mathbf{k}) w_i(\mathbf{k}), \quad \partial_i \varepsilon(\mathbf{k}) = \frac{B_i(\mathbf{k})}{\varepsilon(\mathbf{k})}. \quad (\text{S99})$$

For this two-band model the only nonzero Berry-curvature and orbital-moment component is the out-of-plane one. Using Eqs. (S65) and (S66), one finds

$$\Omega_z^{(s)}(\mathbf{k}) = s \frac{\lambda v^2 w(\mathbf{k})}{\varepsilon(\mathbf{k})^3}, \quad m_z(\mathbf{k}) = \frac{e \lambda v^2 w(\mathbf{k})}{\hbar \varepsilon(\mathbf{k})^2}, \quad (\text{S100})$$

which satisfy the two-band identity

$$m_z(\mathbf{k}) = \frac{e \Delta_s(\mathbf{k})}{2\hbar} \Omega_z^{(s)}(\mathbf{k}). \quad (\text{S101})$$

The sign of  $\Delta_s = 2s\varepsilon$  cancels the sign of  $\Omega_z^{(s)} \propto s$ , so  $m_z^{(+)}(\mathbf{k}) = m_z^{(-)}(\mathbf{k}) \equiv m_z(\mathbf{k})$  is  $s$ -independent and the band index can be dropped without ambiguity. In polar coordinates,  $k_x = k \cos \phi$  and  $k_y = k \sin \phi$ , one has

$$w(\mathbf{k}) = k^3 \cos 3\phi, \quad (\text{S102})$$

so that

$$\Omega_z^{(s)}(k, \phi) = s \frac{\lambda v^2 \cos 3\phi}{(v^2 + \lambda^2 k^4 \cos^2 3\phi)^{3/2}}, \quad m_z(k, \phi) = \frac{e \lambda v^2 k \cos 3\phi}{\hbar (v^2 + \lambda^2 k^4 \cos^2 3\phi)}. \quad (\text{S103})$$

The usual two-band quantum metric is

$$g_{ij}(\mathbf{k}) = \frac{1}{4\varepsilon(\mathbf{k})^4} \left[ \varepsilon(\mathbf{k})^2 (v^2 \delta_{ij} + \lambda^2 w_i w_j) - B_i(\mathbf{k}) B_j(\mathbf{k}) \right], \quad i, j \in \{x, y\}, \quad (\text{S104})$$

namely

$$\begin{aligned} g_{xx} &= \frac{\varepsilon^2 (v^2 + \lambda^2 w_x^2) - B_x^2}{4\varepsilon^4}, \\ g_{yy} &= \frac{\varepsilon^2 (v^2 + \lambda^2 w_y^2) - B_y^2}{4\varepsilon^4}, \\ g_{xy} = g_{yx} &= \frac{\varepsilon^2 \lambda^2 w_x w_y - B_x B_y}{4\varepsilon^4}. \end{aligned} \quad (\text{S105})$$

The band-normalized metric of Eq. (S58) is therefore

$$\mathcal{G}_{ij}^{(s)}(\mathbf{k}) = \frac{2}{\Delta_s(\mathbf{k})} g_{ij}(\mathbf{k}) = \frac{s}{\varepsilon(\mathbf{k})} g_{ij}(\mathbf{k}), \quad (\text{S106})$$

where we used  $\Delta_s = 2s\varepsilon$  and  $s^2 = 1$ . Its derivative is

$$\partial_l \mathcal{G}_{jk}^{(s)} = s \left[ \frac{\partial_l g_{jk}}{\varepsilon} - \frac{g_{jk} B_l}{\varepsilon^3} \right], \quad (\text{S107})$$

and the lowered-index Christoffel combination defined in Eq. (S57) becomes

$$\Gamma_{c,ab}^{(G,s)} = \frac{s}{2} \left[ \frac{\partial_a g_{bc} + \partial_b g_{ac} - \partial_c g_{ab}}{\varepsilon} - \frac{g_{bc} B_a + g_{ac} B_b - g_{ab} B_c}{\varepsilon^3} \right]. \quad (\text{S108})$$

Equivalently,

$$\Gamma_{j,lk}^{(G,s)} + \Gamma_{k,lj}^{(G,s)} = \partial_l \mathcal{G}_{jk}^{(s)}. \quad (\text{S109})$$

The band velocity entering the low-frequency formulas is

$$v_i^{(s)}(\mathbf{k}) = \frac{1}{\hbar} \partial_i \varepsilon_s(\mathbf{k}) = \frac{1}{\hbar} \left( \frac{k_i}{m^*} + s \frac{B_i(\mathbf{k})}{\varepsilon(\mathbf{k})} \right). \quad (\text{S110})$$

Because Eq. (S93) is a continuum model rather than a periodic lattice Hamiltonian, the Brillouin-zone integrals in Eqs. (S60) through (S62) should be understood as continuum momentum integrals with an ultraviolet cutoff  $\Lambda$ .

For the metric contribution, Eq. (S61) together with  $\mathcal{G}_{jk}^{(s)} = s g_{jk}/\varepsilon$  and

$$\partial_l m_z = \frac{e\lambda v^2}{\hbar} \left[ \frac{w_l}{\varepsilon^2} - \frac{2w_l B_l}{\varepsilon^4} \right] \quad (\text{S111})$$

gives the explicit form

$$\beta_{zjkl}^{(G)} = \frac{e^4 \tau \lambda v^2}{2\hbar^2} \sum_{s=\pm} s \int_{\Lambda} g_{jk}(\mathbf{k}) \left[ \frac{w_l(\mathbf{k})}{\varepsilon(\mathbf{k})^3} - \frac{2w(\mathbf{k}) B_l(\mathbf{k})}{\varepsilon(\mathbf{k})^5} \right] f'_0(\varepsilon_s). \quad (\text{S112})$$

For the transport contribution, Eq. (S72) together with the two-band identity

$$\Delta_s(\mathbf{k}) \Omega_z^{(s)}(\mathbf{k}) = 2\lambda v^2 \frac{w(\mathbf{k})}{\varepsilon(\mathbf{k})^2} \quad (\text{S113})$$

gives directly

$$\beta_{zjkl}^{(\text{tr})} = \frac{e^4 \tau^3 \lambda v^2}{\hbar^4} \sum_{s=\pm} \int_{\Lambda} f_0(\varepsilon_s) \partial_j \partial_k \partial_l \left[ \frac{w(\mathbf{k})}{\varepsilon(\mathbf{k})^2} \right]. \quad (\text{S114})$$

The mixed-quadrupole contribution is formal at the level of the continuum model in Eq. (S93). For a two-band system with partner band  $\bar{s} = -s$ , one may write

$$\begin{aligned} \mathcal{Q}_{\alpha\beta\gamma}^{(s)} = & \text{Re} \left[ U_{\alpha\beta\gamma}^{s\bar{s}} [R, C] + U_{\alpha\beta\gamma}^{s\bar{s}} [C, R] + U_{\beta\alpha\gamma}^{s\bar{s}} [R, C] + U_{\beta\alpha\gamma}^{s\bar{s}} [C, R] \right. \\ & \left. - U_{\beta\gamma\alpha}^{s\bar{s}} [R, C] - U_{\beta\gamma\alpha}^{s\bar{s}} [C, R] \right], \end{aligned} \quad (\text{S115})$$

with

$$R_i^{s\bar{s}} = \frac{A_i^{s\bar{s}}}{\Delta_s}, \quad C_z^{s\bar{s}} = -\frac{m_z^{s\bar{s}}}{\Delta_s}, \quad H_{zjk}^{(s)} = -\frac{1}{2} \left( \mathcal{Q}_{jkz}^{(s)} + \mathcal{Q}_{kjk}^{(s)} \right). \quad (\text{S116})$$

For a strict two-band model the genuine third-band  $V$  sum in Eq. (S42) is empty after diagonal-connection terms have been absorbed into the covariant derivative, so a closed form for  $\mathcal{Q}_{\alpha\beta\gamma}^{(s)}$  and  $H_{zjk}^{(s)}$  requires the explicit interband magnetic matrix element  $m_z^{s\bar{s}}$ , that is, a magnetic-coupling prescription for the model Hamiltonian or a lattice regularization that fixes it. Accordingly, the mixed-quadrupole contribution is

$$\beta_{zjkl}^{(H)} = -e^3 \tau \sum_{s=\pm} \int_{\Lambda} H_{zjk}^{(s)}(\mathbf{k}) v_l^{(s)}(\mathbf{k}) f'_0(\varepsilon_s). \quad (\text{S117})$$

For the model Hamiltonian in Eq. (S93), the coefficient

$$\chi \equiv \beta_{zxxy} = \beta_{zyyx} = \beta_{zyxx} = -\beta_{zyyy}$$

defining the  $\sin 3\phi$  harmonic in Eq. (S92) vanishes contribution by contribution. Under  $k_x \rightarrow -k_x$  one has

$$w(-k_x, k_y) = -w(k_x, k_y), \quad \varepsilon_s(-k_x, k_y) = \varepsilon_s(k_x, k_y),$$

so that

$$\Omega_z^{(s)}(-k_x, k_y) = -\Omega_z^{(s)}(k_x, k_y), \quad m_z(-k_x, k_y) = -m_z(k_x, k_y),$$

whereas  $\mathcal{G}_{xx}^{(s)}$ ,  $v_y^{(s)}$ , and  $f_0^{(n)}(\varepsilon_s)$  are even. Therefore

$$\chi_H \equiv \beta_{zxxxy}^{(H)} = 0, \quad \chi_G \equiv \beta_{zxxxy}^{(G)} = 0, \quad \chi_{\text{tr}} \equiv \beta_{zxxxy}^{(\text{tr})} = 0. \quad (\text{S118})$$

The nonzero cubic response is carried by the rotated independent coefficient

$$\bar{\chi}_X \equiv \beta_{zxxx}^{(X)} = -\beta_{zyxy}^{(X)} = -\beta_{zyxy}^{(X)} = -\beta_{zyxy}^{(X)}, \quad X \in \{H, G, \text{tr}\}, \quad (\text{S119})$$

so that the total  $\bar{\chi} = \bar{\chi}_H + \bar{\chi}_G + \bar{\chi}_{\text{tr}}$  produces the  $\cos 3\phi$  response of Eq. (S94). To write these coefficients explicitly, define

$$D(\mathbf{k}) = v^2(k_x^2 + k_y^2) + \lambda^2 w(\mathbf{k})^2, \quad (\text{S120})$$

so that  $\varepsilon(\mathbf{k}) = \sqrt{D(\mathbf{k})}$ , with  $B_x(\mathbf{k})$  given by Eq. (S99). The local orbital moment and the  $xx$  component of the band-normalized metric are

$$m_z(\mathbf{k}) = \frac{e\lambda v^2}{\hbar} \frac{w(\mathbf{k})}{D(\mathbf{k})}, \quad \mathcal{G}_{xx}^{(s)}(\mathbf{k}) = \frac{s[D(\mathbf{k})(v^2 + \lambda^2 w_x(\mathbf{k})^2) - B_x(\mathbf{k})^2]}{4D(\mathbf{k})^{5/2}}. \quad (\text{S121})$$

Hence the metric-contribution coefficient becomes

$$\bar{\chi}_G = \beta_{zxxx}^{(G)} = \frac{e^4 \tau \lambda v^2}{8\hbar^2} \sum_{s=\pm} s \int_{\Lambda} \frac{[w_x(\mathbf{k})D(\mathbf{k}) - 2w(\mathbf{k})B_x(\mathbf{k})][D(\mathbf{k})(v^2 + \lambda^2 w_x(\mathbf{k})^2) - B_x(\mathbf{k})^2]}{D(\mathbf{k})^{9/2}} f_0'(\varepsilon_s). \quad (\text{S122})$$

The transport coefficient is

$$\bar{\chi}_{\text{tr}} = \beta_{zxxx}^{(\text{tr})} = \frac{e^4 \tau^3 \lambda v^2}{\hbar^4} \sum_{s=\pm} \int_{\Lambda} f_0(\varepsilon_s) \partial_x^3 \left[ \frac{w(\mathbf{k})}{D(\mathbf{k})} \right]. \quad (\text{S123})$$

Finally, using  $H_{zxx}^{(s)}(\mathbf{k}) = -\mathcal{Q}_{xxz}^{(s)}(\mathbf{k})$  and  $v_x^{(s)}(\mathbf{k}) = \hbar^{-1}[k_x/m^* + s B_x(\mathbf{k})/\sqrt{D(\mathbf{k})}]$ , the mixed-quadrupole coefficient is

$$\bar{\chi}_H = \beta_{zxxx}^{(H)} = e^3 \tau \sum_{s=\pm} \int_{\Lambda} \mathcal{Q}_{xxz}^{(s)}(\mathbf{k}) v_x^{(s)}(\mathbf{k}) f_0'(\varepsilon_s). \quad (\text{S124})$$

This is the explicit integral form of the mixed-quadrupole coefficient for the model. Given a magnetic coupling for the interband element  $C_{\mu\nu}^z = -m_{\mu\nu}^z/\Delta_{\nu\mu}$ , the numerical recipe is to compute

$$m_{\mu\nu}^z(\mathbf{k}) = \frac{ie}{2\hbar} \epsilon_{zab} \langle \partial_a u_\mu | [h(\mathbf{k}) - \frac{1}{2}(\varepsilon_\mu + \varepsilon_\nu)] | \partial_b u_\nu \rangle, \quad (\text{S125})$$

form  $C_{s\bar{s}}^z = -m_{s\bar{s}}^z/\Delta_s$  and  $R_{s\bar{s}}^x = A_{s\bar{s}}^x/\Delta_s$ , and, since the  $V$  sum is empty for a strict two-band model, evaluate

$$\begin{aligned} \mathcal{Q}_{xxz}^{(s)} &= \text{Re}[2U_{xxz}^{s\bar{s}}[R, C] + 2U_{xxz}^{s\bar{s}}[C, R] - U_{xxz}^{s\bar{s}}[R, C] - U_{xxz}^{s\bar{s}}[C, R]], \\ H_{zxx}^{(s)} &= -\mathcal{Q}_{xxz}^{(s)}. \end{aligned} \quad (\text{S126})$$

The covariant derivative in  $U$  is evaluated either analytically from the smooth eigenvectors or numerically by central differences after parallel transporting neighboring eigenvectors. An equivalent check is the finite-field extraction

$$H_{zxx}^{(s)}(\mathbf{k}) = \lim_{E_x \rightarrow 0} \frac{m_z^{(s)}(\mathbf{k}, E_x) - 2m_z^{(s)}(\mathbf{k}, 0) + m_z^{(s)}(\mathbf{k}, -E_x)}{2e^2 E_x^2}, \quad (\text{S127})$$

with  $m_z^{(s)}(\mathbf{k}, E_x)$  evaluated on the field-corrected wave-packet state.

At zero temperature one has  $f'_0(\varepsilon_s) = -\delta(\varepsilon_s)$ , so Eq. (S122) reduces exactly to a Fermi-surface integral. Defining

$$\mathcal{F}_s(\phi) \equiv \{k > 0 \mid \varepsilon_s(k, \phi) = 0\},$$

and the auxiliary integrand (not to be confused with the band-normalized metric  $\mathcal{G}_{jk}^\nu$ )

$$\mathcal{I}(k, \phi) \equiv \frac{[w_x(k, \phi)D(k, \phi) - 2w(k, \phi)B_x(k, \phi)][D(k, \phi)(v^2 + \lambda^2 w_x(k, \phi)^2) - B_x(k, \phi)^2]}{D(k, \phi)^{9/2}},$$

Eq. (S122) becomes

$$\bar{\chi}_G^{T=0} = -\frac{e^4 \tau \lambda v^2}{8\hbar^2 (2\pi)^2} \sum_{s=\pm} s \int_0^{2\pi} d\phi \sum_{\alpha \in \mathcal{F}_s(\phi)} \frac{k_{s,\alpha}(\phi) \mathcal{I}(k_{s,\alpha}(\phi), \phi)}{|\partial_k \varepsilon_s(k_{s,\alpha}(\phi), \phi)|},$$

with

$$\partial_k \varepsilon_s(k, \phi) = \frac{k}{m^*} + s \frac{v^2 + 3\lambda^2 k^4 \cos^2 3\phi}{\sqrt{v^2 + \lambda^2 k^4 \cos^2 3\phi}}.$$

For generic finite  $\lambda$ , the remaining angular integral is not elementary because  $k_{s,\alpha}(\phi)$  is determined implicitly by a sextic equation. In the weak-warping regime  $|\lambda|k_F^2 \ll v$ , Eq. (S122) simplifies to

$$\bar{\chi}_G = -\frac{e^4 \tau \lambda}{32\pi \hbar^2 v} \sum_{s=\pm} s \int_0^\infty \frac{dk}{k^2} f'_0(\varepsilon_s^{(0)}(k)) + O(\lambda^3), \quad \varepsilon_s^{(0)}(k) = \frac{k^2}{2m^*} - \mu + s v k.$$

At  $T = 0$  and  $\mu > 0$ , the positive Fermi roots are

$$k_{F,\pm}^{(0)} = \sqrt{m^* 2v^2 + 2m^* \mu} \mp m^* v, \quad \partial_k \varepsilon_s^{(0)} \Big|_{k_{F,\pm}^{(0)}} = \frac{\sqrt{m^* 2v^2 + 2m^* \mu}}{m^*},$$

so that the  $s = \pm$  contributions, evaluated at  $k_{F,\pm}^{(0)}$ , combine to give

$$\bar{\chi}_G^{T=0} = \frac{e^4 \tau \lambda}{32\pi \hbar^2 \mu^2} + O(\lambda^3). \quad (\text{S128})$$

By contrast, Eq. (S123) is not universal for the continuum model. At small  $\lambda$ ,

$$\frac{w(\mathbf{k})}{\varepsilon(\mathbf{k})^2} = \frac{k_x^3 - 3k_x k_y^2}{v^2(k_x^2 + k_y^2)} + O(\lambda^2),$$

so that

$$\partial_x^3 \left[ \frac{w(\mathbf{k})}{\varepsilon(\mathbf{k})^2} \right] = \frac{24 k_y^2 (k_x^4 - 6k_x^2 k_y^2 + k_y^4)}{v^2 (k_x^2 + k_y^2)^4} + O(\lambda^2),$$

which is scale free in the continuum regime and behaves as  $1/k^2$ . The two-dimensional continuum integral in Eq. (S123) is therefore cutoff sensitive and cannot be reduced to a unique cutoff-independent number from Eq. (S93) alone. It is best written as

$$\bar{\chi}_{\text{tr}} = \frac{e^4 \tau^3 \lambda}{\hbar^4} \mathcal{C}_{\text{tr}}(m^*, v, \mu, \Lambda, \text{regularization}), \quad (\text{S129})$$

with  $\mathcal{C}_{\text{tr}}$  a nonuniversal dimensionless number fixed only after specifying the lattice completion or ultraviolet regularization of the continuum model.

The dimensionless model curves use the low-energy units  $\hbar = e = v = m^* = 1$ , and the lattice figure additionally sets  $a = 1$ . The vertical axis is  $|\bar{\chi}_X|$  itself, not  $|\bar{\chi}_X/\lambda|$ , and the weak-warping factor  $\lambda$  is retained explicitly, with the dashed guide in the metric plot given by  $\bar{\chi}_G = \lambda/(32\pi\mu^2)$ . In relaxation-time scans the band-geometry integral is fixed and only the explicit  $\tau$  or  $\tau^3$  prefactor is varied.

Finally, Eq. (S124) reduces to the Fermi surface at  $T = 0$ ,

$$\bar{\chi}_H^{T=0} = -\frac{e^3 \tau}{(2\pi)^2} \sum_{s=\pm} \int_0^{2\pi} d\phi \sum_{\alpha \in \mathcal{F}_s(\phi)} \frac{k_{s,\alpha}(\phi) \mathcal{Q}_{xxz}^{(s)}(k_{s,\alpha}(\phi), \phi) v_x^{(s)}(k_{s,\alpha}(\phi), \phi)}{|\partial_k \varepsilon_s(k_{s,\alpha}(\phi), \phi)|}. \quad (\text{S130})$$

This is the most explicit form available within the continuum model. Thus only  $\bar{\chi}_G$  has a universal weak-warping continuum coefficient. The coefficient  $\bar{\chi}_{\text{tr}}$  requires an ultraviolet regularization, and  $\bar{\chi}_H$  requires a microscopic magnetic-coupling prescription or a lattice completion.

### S8. TRIANGULAR-LATTICE REGULARIZATION OF THE $C_{3v}$ MODEL

The continuum model in Eq. (S93) leaves the two issues noted above, namely the magnetic-coupling input required by the mixed-quadrupole contribution and the cutoff dependence of the transport coefficient. Both are removed by a minimal periodic two-band completion on the triangular Bravais lattice, in the same spirit as the hexagonal-warping lattice completion of Ref. [28] and the symmetry-based nonlinear-transport lattice models of Ref. [19]. We therefore place one effective spin-1/2 doublet

$$\Psi_{\mathbf{R}} = (c_{\mathbf{R}\uparrow}, c_{\mathbf{R}\downarrow})^T$$

on each lattice site, with the Pauli matrices acting in this pseudospin space. This is the minimal time-reversal-symmetric realization of Eq. (S93).

The triangular Bravais lattice is generated by

$$\mathbf{a}_1 = a(1, 0), \quad \mathbf{a}_2 = a\left(\frac{1}{2}, \frac{\sqrt{3}}{2}\right), \quad (\text{S131})$$

and it is convenient to choose the three positive nearest-neighbor bonds as

$$\boldsymbol{\delta}_1 = \mathbf{a}_1, \quad \boldsymbol{\delta}_2 = \mathbf{a}_2, \quad \boldsymbol{\delta}_3 = \mathbf{a}_2 - \mathbf{a}_1 = a\left(-\frac{1}{2}, \frac{\sqrt{3}}{2}\right), \quad (\text{S132})$$

with  $\hat{\boldsymbol{\delta}}_n \equiv \boldsymbol{\delta}_n/a$ . A convenient tight-binding representative is

$$H_{\Delta} = H_0 + H_R + H_w, \quad (\text{S133})$$

$$H_0 = \Delta_0 \sum_{\mathbf{R}} \Psi_{\mathbf{R}}^{\dagger} \Psi_{\mathbf{R}} - t \sum_{\mathbf{R}, n} \left( \Psi_{\mathbf{R}}^{\dagger} \Psi_{\mathbf{R}+\boldsymbol{\delta}_n} + \text{h.c.} \right), \quad (\text{S134})$$

$$H_R = i \sum_{\mathbf{R}, n} \Psi_{\mathbf{R}}^{\dagger} \left[ (\hat{\mathbf{z}} \times \hat{\boldsymbol{\delta}}_n) \cdot \boldsymbol{\sigma} \right] \left( t_1 \Psi_{\mathbf{R}+\boldsymbol{\delta}_n} + t_2 \Psi_{\mathbf{R}+2\boldsymbol{\delta}_n} \right) + \text{h.c.}, \quad (\text{S135})$$

$$H_w = it_3 \sum_{\mathbf{R}} \Psi_{\mathbf{R}}^{\dagger} \sigma_z \left( \Psi_{\mathbf{R}+2\boldsymbol{\delta}_1} - \Psi_{\mathbf{R}+2\boldsymbol{\delta}_2} + \Psi_{\mathbf{R}+2\boldsymbol{\delta}_3} \right) + \text{h.c.} \quad (\text{S136})$$

Here  $\Delta_0$  is an on-site energy,  $t$  generates the parabolic scalar dispersion,  $t_1$  is the nearest-neighbor Rashba coupling,  $t_2$  is an auxiliary longer-range Rashba term that will be fixed by exact matching, and  $t_3$  is the inversion-breaking third-neighbor warping amplitude. In momentum space,

$$H_{\Delta} = \sum_{\mathbf{k}} \Psi_{\mathbf{k}}^{\dagger} \mathcal{H}_{\Delta}(\mathbf{k}) \Psi_{\mathbf{k}}, \quad \mathcal{H}_{\Delta}(\mathbf{k}) = h_0(\mathbf{k})\sigma_0 + \mathbf{d}(\mathbf{k}) \cdot \boldsymbol{\sigma}, \quad (\text{S137})$$

with  $q_n \equiv \mathbf{k} \cdot \boldsymbol{\delta}_n$ ,

$$h_0(\mathbf{k}) = \Delta_0 - 2t \sum_{n=1}^3 \cos q_n, \quad (\text{S138})$$

$$\mathbf{d}_{\parallel}(\mathbf{k}) = 2 \sum_{n=1}^3 (\hat{\mathbf{z}} \times \hat{\boldsymbol{\delta}}_n) \left[ t_1 \sin q_n + t_2 \sin(2q_n) \right], \quad (\text{S139})$$

$$d_z(\mathbf{k}) = -2t_3 \left[ \sin(2q_1) - \sin(2q_2) + \sin(2q_3) \right]. \quad (\text{S140})$$

With the standard time-reversal operator  $\mathcal{T} = i\sigma_y K$ , one has  $\mathcal{T}\mathcal{H}_\Delta(\mathbf{k})\mathcal{T}^{-1} = \mathcal{H}_\Delta(-\mathbf{k})$ , while inversion is broken by the odd pseudospin-dependent harmonics.

Expanding near  $\Gamma$  gives

$$h_0(\mathbf{k}) = (\Delta_0 - 6t) + \frac{3ta^2}{2}(k_x^2 + k_y^2) + \mathcal{O}(k^4), \quad (\text{S141})$$

$$\mathbf{d}_\parallel(\mathbf{k}) = 3a(t_1 + 2t_2)(k_x\hat{\mathbf{y}} - k_y\hat{\mathbf{x}}) - 3a^3\left(\frac{t_1}{8} + t_2\right)(k_x^2 + k_y^2)(k_x\hat{\mathbf{y}} - k_y\hat{\mathbf{x}}) + \mathcal{O}(k^5), \quad (\text{S142})$$

$$d_z(\mathbf{k}) = 2a^3t_3(k_x^3 - 3k_xk_y^2) + \mathcal{O}(k^5). \quad (\text{S143})$$

Equations (S142) and (S143) show that a nearest-neighbor Rashba term by itself generates an unwanted isotropic cubic correction proportional to  $k^2(k_x\sigma_y - k_y\sigma_x)$ . Exact reproduction of Eq. (S93) through cubic order therefore requires

$$t_2 = -\frac{t_1}{8}. \quad (\text{S144})$$

This constraint does not add a new low-energy parameter. It merely fixes the auxiliary longer-range Rashba amplitude. Matching the remaining coefficients to Eq. (S93) gives

$$t = \frac{1}{3m^*a^2}, \quad t_1 = \frac{4v}{9a}, \quad t_2 = -\frac{v}{18a}, \quad t_3 = \frac{\lambda}{2a^3}, \quad \Delta_0 = 6t - \mu. \quad (\text{S145})$$

The resulting Bloch Hamiltonian obeys

$$\mathcal{H}_\Delta(\mathbf{k}) = \left(\frac{k_x^2 + k_y^2}{2m^*} - \mu\right)\sigma_0 + v(k_x\sigma_y - k_y\sigma_x) + \lambda(k_x^3 - 3k_xk_y^2)\sigma_z + \dots, \quad (\text{S146})$$

where the omitted terms begin at  $\mathcal{O}(k^4)$  in the scalar channel and  $\mathcal{O}(k^5)$  in the Pauli-vector channel. Equation (S146) is therefore an exact  $\Gamma$ -point regularization of Eq. (S93) to the order retained in the continuum model.

The two lattice bands are

$$\varepsilon_s(\mathbf{k}) = h_0(\mathbf{k}) + s\varepsilon(\mathbf{k}), \quad \varepsilon(\mathbf{k}) = |\mathbf{d}(\mathbf{k})|, \quad P_s(\mathbf{k}) = \frac{1 + s\hat{\mathbf{d}}(\mathbf{k}) \cdot \boldsymbol{\sigma}}{2}, \quad s = \pm,$$

with  $\hat{\mathbf{d}} = \mathbf{d}/\varepsilon$ . Because  $\mathcal{H}_\Delta(\mathbf{k})$  is a finite  $2 \times 2$  Bloch matrix on a compact Brillouin zone, the Berry curvature, quantum metric, orbital moment, and interband matrix elements entering Eqs. (S115) and (S116) are all fixed unambiguously. Standard two-band formulas give [47]

$$\Omega_s^z(\mathbf{k}) = -\frac{s}{2\varepsilon(\mathbf{k})^3} \mathbf{d} \cdot \left(\partial_{k_x}\mathbf{d} \times \partial_{k_y}\mathbf{d}\right), \quad g_{ij}^{(s)}(\mathbf{k}) = \frac{1}{4} \partial_i\hat{\mathbf{d}} \cdot \partial_j\hat{\mathbf{d}}, \quad m_s^z(\mathbf{k}) = \frac{e}{\hbar} [\varepsilon_s(\mathbf{k}) - h_0(\mathbf{k})] \Omega_s^z(\mathbf{k}). \quad (\text{S147})$$

The interband orbital matrix element  $m_z^{s\bar{s}}(\mathbf{k})$ , and hence  $C_z^{s\bar{s}}$ ,  $\mathcal{Q}_{\alpha\beta\gamma}^{(s)}$ , and  $H_{zjk}^{(s)}$ , then follow directly from the same eigenvectors via Eqs. (S125) through (S126), so the previously formal mixed-quadrupole contribution becomes a definite Brillouin-zone integral.

A practical numerical workflow is straightforward. The reciprocal lattice vectors are

$$\mathbf{b}_1 = \frac{2\pi}{a} \left(1, -\frac{1}{\sqrt{3}}\right), \quad \mathbf{b}_2 = \frac{2\pi}{a} \left(0, \frac{2}{\sqrt{3}}\right), \quad (\text{S148})$$

and one may sample  $\mathbf{k} = (n_1/N)\mathbf{b}_1 + (n_2/N)\mathbf{b}_2$  on a uniform  $N \times N$  grid with  $N$  between 200 and 500. Diagonalizing  $\mathcal{H}_\Delta(\mathbf{k})$  yields  $\varepsilon_s(\mathbf{k})$  and the cell-periodic eigenvectors, from which one computes  $\Omega_s^z(\mathbf{k})$ ,  $m_s^z(\mathbf{k})$ ,  $g_{ij}^{(s)}(\mathbf{k})$ , and the interband matrix elements entering  $\mathcal{Q}_{\alpha\beta\gamma}^{(s)}$ . The three dc contributions then follow from the compact Brillouin-zone versions of Eqs. (S60) through (S62), or from the finite-frequency ordered formulas in Eq. (S54). In contrast to the continuum model, the transport contribution is now cutoff independent and the weak-warping approximation is optional rather than mandatory. This lattice regularization turns the  $C_{3v}$  continuum model into a fully computable toy model for contribution-resolved numerical comparisons.

Figure S2 validates the triangular-lattice completion. The metric Brillouin-zone integral agrees with the weak-warping continuum prediction at small  $\mu$ , confirming that the lattice Hamiltonian reproduces the continuum  $C_{3v}$  theory near  $\Gamma$ , and the relaxation-time scan reproduces the  $\tau$  and  $\tau^3$  powers. Crucially, the lattice transport coefficient is finite and cutoff independent, unlike its continuum counterpart. The mixed-quadrupole contribution is not plotted, since it requires the separate procedure of Eqs. (S125) through (S126).

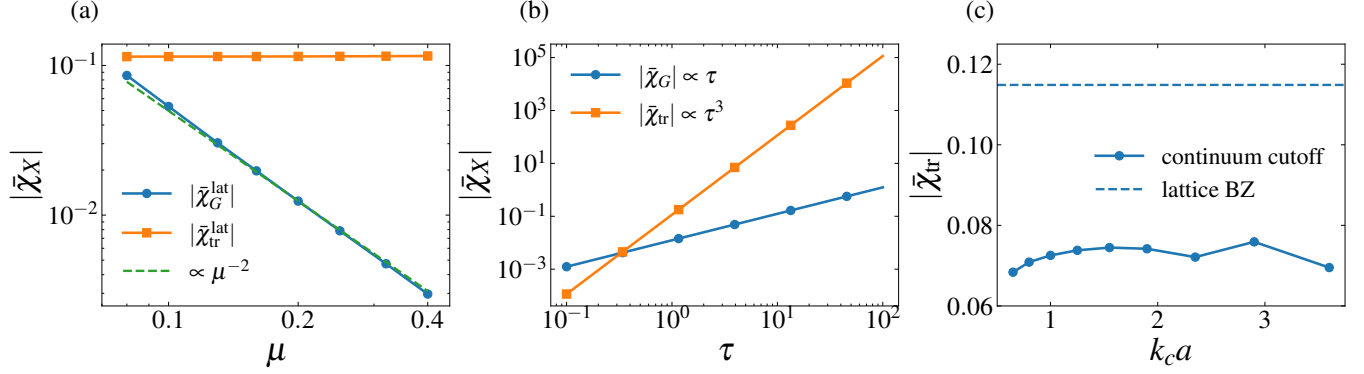


FIG. S2. Triangular-lattice regularization of the  $C_{3v}$  model. The plotted data use  $e = \hbar = a = v = m^* = 1$ ,  $\lambda = 0.05$ , temperature  $T = 0.008$ , a midpoint  $241 \times 241$  Brillouin-zone grid, and finite-difference step  $2 \times 10^{-3}$ . Panel (a) uses  $\tau = 1$  and  $\mu = 0.08, 0.10, 0.13, 0.16, 0.20, 0.25, 0.32, 0.40$ . The dashed guide is the weak-warping continuum prediction  $\bar{\chi}_G = \lambda/(32\pi\mu^2)$ . The computed values at  $\mu = 0.20$  are  $|\bar{\chi}_G^{\text{lat}}| = 1.24 \times 10^{-2}$  and  $|\bar{\chi}_{\text{tr}}^{\text{lat}}| = 1.15 \times 10^{-1}$ . Panel (b) fixes  $\mu = 0.20$  and varies  $\tau$  from  $10^{-1}$  to  $10^2$ , showing  $|\bar{\chi}_G| \propto \tau$  and  $|\bar{\chi}_{\text{tr}}| \propto \tau^3$ . Panel (c) compares the lattice value with a continuum transport integral using the soft cutoff  $\exp[-(k/k_c)^2]$  on a  $301 \times 301$  grid, for  $k_c a = 0.65, 0.80, 1.00, 1.25, 1.55, 1.90, 2.35, 2.90, 3.60$ .

## S9. EXPERIMENTAL SIGNATURES OF CUBIC NONLINEAR MAGNETIZATION

This section translates the theoretical results into experimentally accessible observables. We focus on the angular fingerprint of the cubic tensor, THG-MOKE as the detection platform, separation of the three quantum-geometric contributions through frequency and relaxation-time scaling, and candidate material classes.

### A. Angular fingerprint and polarimetric detection

The cleanest experimental handle on the cubic magnetization tensor is its characteristic dependence on the azimuthal orientation  $\phi$  of the driving electric field. For a  $C_{3v}$ -symmetric sample with the mirror plane along  $\hat{x}$  and an in-plane field  $\mathbf{E}_\omega = E_0(\cos \phi, \sin \phi, 0)$ , Eqs. (S91) and (S92) give the out-of-plane magnetization  $M_z^{(3)} = \chi E_0^3 \sin 3\phi$ , or  $\bar{\chi} E_0^3 \cos 3\phi$  in the rotated convention of the model Hamiltonian (S93). A full  $\phi$  scan of  $M_z$  at fixed  $E_0$  constitutes the angular fingerprint measurement.

### B. THG-MOKE as an experimental platform

The cubic magnetization  $M_i^{(3)} \propto E_j E_k E_l$  can be probed directly by third-harmonic magneto-optical Kerr spectroscopy [24, 82]. In a THG-MOKE measurement one drives the system at a single frequency  $\omega$  and reads out the third-harmonic component of the magnetization at  $\Omega = 3\omega$ . This output channel probes the frequency-resolved tensor  $\beta_{ijkl}^{\text{phys}}(3\omega, \omega, \omega, \omega)$  and measures a coherent cubic magnetization rather than a contribution-resolved observable. The dc expressions used in the main text are the leading quasi-static limit of this tensor. When  $\omega\tau \gtrsim 1$  or when interband resonances are approached, the ordered finite-frequency denominators in Eqs. (S152) through (S154) must be retained. In the single- $\tau$  regime the two geometric contributions  $\beta^{(H)}$  and  $\beta^{(G)}$  are both linear in  $\tau$  and are therefore favored over the  $\tau^3$  transport contribution at moderate disorder. Separating the mixed quadrupole from the metric contribution requires the gate and two-color frequency diagnostics described below. This configuration is the natural cubic counterpart of the SHG-MOKE methodology recently used by Qian *et al.* [24] to detect a second-order quantum-geometric magnetization in  $\text{WTe}_2$ . The same calibrated SMOKE setup can be returned from  $2\omega$  readout to  $3\omega$  readout.

The measured Kerr rotation is proportional to the magneto-optical source at the emitted frequency, but the proportionality factor is sample-geometry dependent. A safe way to write the extraction is

$$\theta_K(3\omega) + i\eta_K(3\omega) = \mathcal{F}(3\omega, n_s, d, \sigma_{\text{opt}}, \dots) M_z^{(3)}(3\omega), \quad (\text{S149})$$

where  $\mathcal{F}$  is obtained from the optical transfer matrix, including substrate index  $n_s$ , film thickness  $d$ , sheet or bulk optical conductivities, and boundary conditions. In the idealized normal-incidence bulk limit in Gaussian units, this

reduces schematically to the familiar magneto-optical estimate [56–58]

$$\theta_K + i\eta_K \simeq \frac{4\pi}{c} \frac{M_z^{(3)}}{n^2 - 1}, \quad (\text{S150})$$

with complex refractive index  $n$ . For a topological-insulator surface state,  $M_z^{(3)}$  is a sheet magnetization rather than a bulk density. One may quote an effective bulk value by dividing by an optical thickness, but quantitative extraction should include the sheet response as a boundary condition in the transfer matrix. Substituting  $M_z^{(3)} = \bar{\chi} E_0^3 \cos 3\phi$  gives a Kerr signal that can be read out by rotating the linear polarization of the pump laser.

### C. Frequency and relaxation-time scaling as contribution diagnostics

The three dc contributions carry distinct powers of the relaxation time  $\tau$  and distinct frequency denominators in the low-frequency tensor of Eq. (S55). These differences constitute independent diagnostics.

*$\tau$ -scaling.* From Eqs. (S60) through (S62)

$$\beta^{(H)} \propto e^3 \tau, \quad \beta^{(G)} \propto e^3 \tau, \quad \beta^{(\text{tr})} \propto e^3 \tau^3. \quad (\text{S151})$$

At low disorder ( $\tau$  large), the transport contribution ( $\tau^3$ ) can dominate. At higher disorder ( $\tau$  small), the mixed-quadrupole and metric contributions ( $\tau^1$ ) are favored. Measuring the cubic magnetization as a function of sample purity, for example by varying temperature or controlled impurity doping, can therefore separate the contributions. The slope of  $\ln |\bar{\chi}|$  versus  $\ln \tau$  crosses over from 3 in the clean transport-dominated limit to 1 in the geometric-contribution-dominated limit. Side-jump, skew-scattering, multiband vertex corrections, and energy-dependent lifetimes can change the quantitative scaling in real samples. In particular, side-jump contributions are typically  $\tau$ -independent and could mimic an apparent geometric scaling in the moderate-disorder window, whereas skew-scattering produces  $\tau$ -dependent extrinsic pieces whose exponents depend on the dominant scattering mechanism. The clean separation in Eq. (S151) should therefore be regarded as the reference structure of the intrinsic response, and is most reliably tested when combined with the cutoff-independent gate dependence  $\bar{\chi}_G \propto \mu^{-2}$  derived below and with non-degenerate two-color frequency scans, both of which are insensitive to the lifetime in different ways. Analogous intrinsic-versus-extrinsic discussions in the nonlinear Hall context [15, 16, 22] confirm that this diagnostic is informative but not decisive on its own.

*Frequency denominators.* From Eq. (S55), the three surviving contributions at finite frequency carry the Drude-like denominators

$$\beta^{(H)} \propto \frac{1}{1 - i\omega_3 \tau}, \quad (\text{S152})$$

$$\beta^{(G)} \propto \frac{1}{1 - i\Omega \tau}, \quad (\text{S153})$$

$$\beta^{(\text{tr})} \propto \frac{1}{(1 - i\Omega \tau)[1 - i(\omega_2 + \omega_3)\tau](1 - i\omega_3 \tau)}. \quad (\text{S154})$$

The mixed-quadrupole contribution responds at the frequency of the last field insertion  $\omega_3$ , while the metric contribution responds at the total output frequency  $\Omega$ . These rolloffs refer to the ordered kernel at fixed  $(j, \omega_1), (k, \omega_2), (l, \omega_3)$ . The physical THG response is obtained by the symmetrization in Eq. (S15), which averages over which input leg carries which Cartesian index. For a degenerate single-color drive,  $\omega_1 = \omega_2 = \omega_3 = \omega$  and  $\Omega = 3\omega$ . The resulting onset scales are therefore at  $\omega$  for the mixed quadrupole, at  $3\omega$  for the metric contribution, and at  $\omega, 2\omega,$  and  $3\omega$  for the transport contribution. The denominators should not be interpreted as suppressing the transport contribution in the strict  $\omega\tau \ll 1$  limit. There all denominators approach unity and the dc powers in Eq. (S151) control the hierarchy. Their diagnostic value is in the rolloff regime  $\omega\tau \gtrsim 1$ , where the transport contribution contains two additional Drude factors relative to the metric contribution and one additional factor relative to the mixed-quadrupole contribution. Non-degenerate two-color or three-color configurations give a substantially cleaner separation because  $\omega_3, \omega_2 + \omega_3,$  and  $\Omega$  can be tuned independently, allowing the per-contribution rolloffs to be measured one at a time rather than as a sum.

*Temperature dependence.* At low temperatures  $T \ll \mu$ , the Fermi-surface integrals in Eqs. (S63) and (S64) are essentially temperature-independent, and the only  $T$ -dependence enters through  $\tau(T)$  via electron-phonon scattering. In the two-band weak-warping limit the metric contribution reduces to Eq. (S128),  $\bar{\chi}_G^{T=0} \propto \lambda/\mu^2$ , so varying the chemical potential by gating or doping should produce a  $\mu^{-2}$  dependence of the metric contribution to the cubic MOKE signal.

#### D. Background discrimination and inverse-Faraday contributions

Any THG-MOKE measurement of cubic orbital magnetization must control for several backgrounds, namely ordinary optical third-harmonic generation, inverse-Faraday effects, drive-induced Oersted fields, and bolometric heating. We collect here the discriminants that distinguish the intrinsic cubic magnetization from each. The angular fingerprint  $\cos 3\phi$  or  $\sin 3\phi$  is itself a strong filter, because most backgrounds are isotropic in  $\phi$  on a  $C_{3v}$  surface. The phase-sensitive Kerr response and the strict  $E_0^3$  power law provide two further independent handles. The usual inverse-Faraday source is proportional to  $\text{Im} \mathbf{E}_\omega \times \mathbf{E}_\omega^*$  and is quadratic in the optical field. It can affect a third-harmonic measurement only through additional mixing or field-induced changes. It vanishes identically for a linearly polarized drive, while the intrinsic cubic magnetization studied here is finite for linear polarization. Comparing linear and circular polarizations is thus a direct discriminant. A  $\cos 3\phi$  angular pattern that persists for purely linear polarization and tracks the predicted  $\mu^{-2}$  gating cannot be the usual inverse-Faraday response. Drive-induced Oersted fields are similarly polarization sensitive and additionally depend on sample geometry, while bolometric heating is broadband, slow, and lacks the  $C_{3v}$  angular harmonic. A background that simultaneously reproduces the  $C_{3v}$  angular harmonic with linear polarization, the cubic power law in  $E_0$ , the gate-tunable  $\mu^{-2}$  trend of the metric contribution, and the predicted intrinsic  $\tau$  scaling in a disorder scan is implausible.

#### E. Order-of-magnitude estimate of the THG-MOKE signal

It is useful to give a rough estimate of the expected Kerr rotation in the most direct platform. For a  $\text{Bi}_2\text{Te}_3$  surface state with hexagonal warping  $\lambda \sim 2.5 \times 10^{-28} \text{ eV m}^3$ , surface velocity  $v \sim 4 \times 10^5 \text{ m s}^{-1}$ , chemical potential  $\mu \sim 0.1 \text{ eV}$  measured from the Dirac point, and a transport lifetime  $\tau \sim 10^{-13} \text{ s}$ , Eq. (S128) gives  $\bar{\chi}_G \simeq 9 \times 10^{-30} \text{ A (V/m)}^{-3}$ . Equivalently,  $M_z^{(3)}/E_0^3 \sim 10^{-18} \mu_B \text{ nm}^{-2} (\text{V/cm})^{-3}$ . Under a THz drive at  $E_0 \sim 10^4 \text{ V cm}^{-1}$ , this produces  $M_z^{(3)} \sim 10^{-6} \mu_B \text{ nm}^{-2}$  at  $3\omega$ . Because the signal scales as  $E_0^3$ , a stronger pulsed THz drive with  $E_0 \sim 10^5 \text{ V cm}^{-1}$  would enhance the same estimate by  $10^3$  and give  $M_z^{(3)} \sim 10^{-3} \mu_B \text{ nm}^{-2}$ . The corresponding Kerr scale is enhanced by the same factor, although this high-field estimate should be used only while heating, bolometric response, Oersted fields, and nonperturbative corrections remain controlled. Substituting the baseline  $10^4 \text{ V cm}^{-1}$  estimate into a transfer-matrix calculation with an optical surface thickness of order a nanometer gives a Kerr rotation well below a microradian. The absolute number is sensitive to band-structure detail, optical transfer factors, and surface quality. The gate dependence of the metric channel,  $\mu^{-2}$ , and the polarization comparison against inverse Faraday are more robust than this absolute estimate.

#### F. Candidate material platforms

The most direct platforms are systems in which the angular fingerprint, gate tuning, and disorder or frequency scans are all accessible.  $C_{3v}$  topological-insulator surfaces such as  $\text{Bi}_2\text{Se}_3$  and  $\text{Bi}_2\text{Te}_3$  realize the hexagonally warped Dirac structure of Eq. (S93) [28, 47]. The  $\cos 3\phi$  fingerprint and the gate-controlled  $\mu^{-2}$  metric test are therefore especially transparent. Zincblende or tetrahedral semiconductors provide cubic-leading axial responses from Dresselhaus spin-orbit coupling. Orthorhombic  $T_d$  semimetals such as  $\text{MoTe}_2$  and  $\text{WTe}_2$  and moiré systems with  $C_3$  or  $C_{3v}$  symmetry are useful broader platforms because they already support nonlinear magneto-optical protocols and tunable band geometry, although lower-symmetry quadratic channels may coexist with the cubic signal.

#### G. Summary of experimental predictions

Table S3 summarizes the main experimental predictions.

TABLE S3. Summary of experimental predictions for cubic nonlinear magnetization.  $\tau$  is the scattering time,  $\mu$  the chemical potential, and  $\phi$  the azimuthal angle of the driving field.

Observable	Prediction	Diagnostic	Platform
Angular scan of $M_z$	$\sin 3\phi$ or $\cos 3\phi$ (related by $30^\circ$ rotation)	Identifies $C_{3v}$ symmetry class	TI surface, TMD
Linear vs. circular polarization	Cubic $M_z$ finite for linear usual inverse Faraday vanishes	Rejects inverse-Faraday background Separates mixed-quadrupole/metric from transport,	TI surface TMD
$\tau$ -dependence (intrinsic)	$ \bar{\chi}  \propto \tau$ (geometric), $ \bar{\chi}  \propto \tau^3$ (transport)	extrinsic side-jump/skew can modify quantitative scaling Tests metric contribution	Tunable disorder
Gate-voltage scan	$ \bar{\chi}_G  \propto \mu^{-2}$	formula Eq. (S128), cutoff-independent	TI surface gated
Two-color frequency sweep	$\beta^{(H)}$ Drude rolloff at $\omega_3\tau \sim 1$ , $\beta^{(G)}$ rolloff at $\Omega\tau \sim 1$	Resolves contribution relaxation scales (only non-degenerately)	Two-color THz
THG MOKE	Coherent cubic magnetization response	Cubic ( $\chi^{(3)}$ ) counterpart of the quadratic $\chi^{(2)}$ Christoffel magnetization of Refs. [23, 24]	Noncentrosymmetric metals
Temperature	Tracks contribution Drude factors, mixed-quadrupole/metric $\sim \tau(T)$ , transport $\sim \tau^3(T)$	Maps $e$ -ph scattering to response	Low-T spectroscopy